All-electron mixed basis *GW* calculation of electronic band structure of transition metal oxide

遷移金属酸化物の全電子混合基底*GW*計算

張　　明

12SD292

Zhang Ming

Specialization in Physics,
Department of Physics, Electrical and Computer Engineering,
Graduate School of Engineering,

Yokohama National University

This dissertation is submitted for the degree of
Doctor of Philosophy in Engineering

September 2015

Abstract

Most of the calculations of electronic properties of transition metal oxide have been based on the local density approximation (LDA) in the density-functional theory (DFT). However, because of the well-known deficiency of the LDA, there exists a serious discrepancy between the Kohn-Sham (KS) eigenvalues and the experimental excitation energies. In order to improve the accuracy of electronic structure calculation of materials, the *GW* approximation is introduced on the basis of many-body perturbation theory (MBPT).

Transition metal oxides have unusual and useful electronic and magnetic properties and are used in wide variety of applications. Since many of these properties strongly depend on defects or impurities, it is important to study electronic structures of transition metal oxides with impurities in order to understand the physics of material properties. TiO_2 and ZnO are the most investigated metal oxides for wide variety applications. There exists a quite large degree of uncertainty in the experimental electronic energy gap. It also has been reported with much interest that Nb impurities affect the conductivity and optical properties of rutile TiO_2. It is therefore highly desirable to present a systematic theoretical explanation of their electronic structures.

In this thesis, I used our original all-electron mixed basis code TOMBO to calculate the electronic structure of ZnO, TiO_2 and rutile TiO_2 with Nb impurities. Based on these results, it can be conclude that the *GW* approximation seems good in describing not highly correlated transition metal oxide system and with impurities.

Table of contents

List of figures

List of tables

Chapter 1

Introduction

1.1 The transition metal oxide

Because of the unique band structure properties, the transition metal oxides are in a wide spectrum of electronic and optoelectronic applications. The unusual properties are due to the unique nature of the outer d-electrons. Therefore there exist strongly electron correlation.

Titanium dioxide (TiO_2) is one of the most investigated transition metal oxides for wide variety of photocatalytic, thermoelectric, solar cell, biosensing and gas sensing applications. It exhibits serveral phases. The experimental band gap of anatase TiO_2 is known to be 3.2 eV [1] or 3.4 eV [2]. The experimental band gap of rutile TiO_2 has a quite large degree of uncertainty: 3.0 eV [3, 4], 3.3 ± 0.5 eV [5], 3.6 ± 0.2 eV [6], and 4.0 eV [7].

Zinc oxide (ZnO) is a II-VI compound transition metal oxide, having wide electronic and optoelectronic applications, such as light-emitting diodes, solar cells, and so on. The band gap of cubic zincblende ZnO is 3.44 eV [8, 9] at low temperatures and 3.37 eV at room temperature [9].

Research on TiO_2 and ZnO has continued for many decades, but it is still challenging for understanding the electronic structures. Transition metal oxides have open d electron shells, where electrons occupy narrow orbitals. Electrons experience strong Coulombic repulsion because of their spatial confinement in those orbitals. Most of the calculations of electronic structure of transition metal oxides have been based on the density-functional theory (DFT) [10]. However, the Kohn-Sham (KS) eigenvalues underestimate the band gap compared with the experimental excitation energies, due to the well-known deficiency of the LDA that Kohn-Sham eigenvalues are not quasiparticle energies.

It has been also reported with much interest that Nb impurities affect the conductivity and optical properties of rutile TiO_2 [11, 12]. In thermoelectric applications, for example, $Ti_{1-x}Nb_xO_2$ alloys have attracted experimental interest. Rutile TiO_2 has high Seebeck

coefficient, low thermal conductivity, non-toxicity, and stability at high temperatures, and possesses potential applications in thermoelectric material field. However, the electronic conductivity of rutile TiO_2 is very low, which limits the thermoelectric conversion efficiency. With Nb impurities, the electronic structure will be modified. Modifying the electronic structure is important way to improve physical properties of transition metal oxides. Nb impurites reduce the band gap, and improves the conductivity and optical properties of rutile TiO_2. $Ti_{1-x}Nb_xO_2$ alloys can obtain high electronic conductivity, and improve thermoelectric properties. It is necessarily to stuy the electronic structure of rutile TiO_2 with Nb impurities to explain to physical mechanism. However, DFT results fail and obtain wrong band structure.

To overcome the shortcomings of the standard DFT, many approaches have been introduced, for example the self-interaction correction (SIC)[13], the DFT hybrid approach[14], and the LDA/GGA + U approach[15]. The first approach has a clear physics but it has also a serious ambiguity how to treat crystals. The second approach is widely used but the results strongly depend on the parameter how to mix the DFT and Hartree-Fock functionals. The last approach modifies the intra-atomic Coulomb interaction, improving the accuracy of the electronic structure. However, there exits the Hubbard U parameter that adjusts the band structure. The results with finite U value in the LDA/GGA + U approach sometimes overestimate the lattice parameters and underestimate the band gap[16]. The calculated DFT band structures are not improved by the energy-independent nonlocal-density corrections to the LDA. Therefore, quasiparticle (QP) energies are needed [17]. The GW approximation [17, 18] is introduced to improve the accuracy of electronic structure calculation of finite band-gap systems.

1.2   The motivations for the thesis

The one-shot GW approximation, on the basis of many-body perturbation theory (MBPT) [18, 19], solves the QP equation with the first order perturbative expansion for the self-energy operator using the many-body Green's function. It has been successfully applied for a broad class of materials ranging bulk insulators and semiconductors [18, 19]. Some one-shot GW calculations of TiO_2 and ZnO have been already reported: In anatase TiO_2 calculations, Kang and Hybertsen [20] reported the X-Γ indirect band gap of 3.56 eV. Patrick and Giustino [21] obtained 3.3 eV of GW quasiparticle band gap starting from DFT+U. In rutile TiO_2 calculations, 4.8 eV [22], 3.59 eV [23], and 3.34 eV [20] were reported by the one-shot GW method. Schilfgaarde *et al.* [24, 25] performed full-potential LMTO based self-consistent GW calculation and obtained 3.78 eV for the band gap. Lany [26] used the self-consistent GW calculation with fixed GGA+U wave function and obtained 4.48 eV for

the band gap. He also obtained TDDFT-based local-field corrected values of 3.11 eV and 3.4 eV by introducing empirical d-orbital on-site energy. In zincblende ZnO calculation, Shishkin and Kresse [27, 28] reported 2.12 eV of band gap in one-shot *GW* method, 2.54 eV and 3.0 eV in GW_0 method, and 3.2 eV in *GW* method.

These values of the *GW* band gap are very scattered. There are two main reasons: (1) Local fields [29, 30] play an important role in the calculation of dielectric function $\varepsilon(\omega)$, and can cause a significant reduction of the dielectric function. Within the independent-particle picture, local fields are often included by calculating the entire dielectric matrix $\varepsilon_{\mathbf{G},\mathbf{G'}}(\omega)$ and evaluating the macroscopic dielectric function from the head of the inverse matrix, $\varepsilon_{\mathbf{G},\mathbf{G'}}^{-1}(\omega)$, here $\mathbf{G}$ denotes the reciprocal lattice vectors. Hybertsen and Louie [18, 31] pointed that local field effects (the off-diagonal elements of the dielectric matrix) strongly influence the self-energy. von der Linden and Horsch [32] show that neglecting the off-diagonal elements from the very beginning leads to an almost rigid upwards shift of all valence-band states by about 0.4 eV relative to the conduction bands. There exit strong local filed effects, so the use of the generalized plasmon-pole (GPP) model [18] is not suitable for the electronic structure of transistion metal oxides [20]. In rutile TiO_2 case, for example, it leads to too large band gap. (2) The one-shot *GW* quasiparticle energy is determined by Kohn-Sham eigenvalues and wave functions. Therefore different pseudopotential and exchange-correlation functional may lead to the *GW* band gap differences.

In $Ti_{1-x}Nb_xO_2$ system, the Nb orbitals most likely introduce additional structure in the loss function. In order to obtain an accurate band gap of TiO_2, ZnO and $Ti_{1-x}Nb_xO_2$, we adopt the full ω integration instead of using the GPP model to evaluate the correlation part of the self-energy, and we use the all-electron mixed basis *GW* method, in which wave functions are accuratedly described by plane waves (PWs) and atomic orbitals (AOs). The present approach is capable to describe spatially localized states as well as extended states quite well.

1.3   The aim of the thesis

The aim of the thesis is to achieve an accurate description of the electronic structure of transition metal oxides, and understand how atom doping affect the band gap, using our original all-electron mixed basis code TOMBO.

1. **To obtain accurate electronic structures of ZnO and TiO$_2$**

    There exist strong electronic correlation in transition metal oxides. DFT results fail to describe the electronic structure. Electronic structure of pure ZnO and TiO_2 will be calculated by *GW* method. QP energy will also be discussed, which contributions from

the LDA exchange-correlation potential, V_{xc}^{LDA}, and the exchange (Σ_x) and correlation (Σ_c) parts of the self-energy Σ_{GW} .

2. **To study how the Nb impurity affects the band structure of Ti$_{1-x}$Nb$_x$O$_2$**

   In rutile TiO$_2$ with Nb impurities case, the DFT results obtain wrong band structure. It is necessary to improve the band structure by *GW* method, and discuss how the Nb impurity affects the band structure.

3. **To perform *GW* calculation using TOMBO**

   All calculations will be based on our original all-electron mixed basis code TOMBO [33–36]. In particular we use the new parallel version of TOMBO which includes both the *GW* cluster calculation routine [37] and the *GW* crystal calculation routine [38, 39]. The code is fully parallelized using MPI and openMP with distributed memory architechture. Our method may help understanding the change in the electronic structure of highly correlated transition metal oxide without and with impurities. It is hoped TOMBO will be used by many scientists and engineers in the world and a lot of important results will be obtained by using TOMBO in various fields.

1.4   Outline of the thesis

The outline of the thesis is as follows:

1. **Chapter 1: Introduction**

   In this chapter, it contains an introduction of transition metal oxide, and the motivations of this thesis.

2. **Chapter 2: The *GW* Approximation**

   In this chapter, the *GW* approximation is introduced, in order to improve the accuracy of electronic structure calculation of transition metal oxide.

3. **Chapter 3: Calculation Method**

   A short introduction of TOMBO is presented. The mixed basis formulation and all-electron charge density are also introduced.

4. **Chapter 4: Electronic Structure of anatase TiO$_2$ zincblende and ZnO**

   I perform calculations for pure TiO$_2$ and ZnO, and discuss the quasiparticle (QP) energy contributions from the LDA exchange-correlation potential, and the exchange and correlation parts of the self-energy.

5. **Chapter 5: Electronic Structure of rutile TiO$_2$ with and without Nb impurities**

   In this chapter, I calculate the Nb impurities case, and found an impurity level well localized in the middle of the band gap of the host rutile TiO$_2$, and discuss how the Nb impurity affects the band structure.

6. **Chapter 6: Conclusions and Outlook**

   Based on above results, I outlook *GW* approximation in calculation of band structure, and the TOMBO used in describing not highly correlated transition metal oxide system.

Chapter 2

The *GW* Approximation

The calculated DFT band structures are not improved by the energy-independent nonlocal-density corrections to the LDA, in any case, quasiparticle energies are needed [19]. In order to improve the accuracy of electronic structure calculation of materials, the *GW* approximation is introduced on the basis of many-body perturbation theory (MBPT)[17].

2.1 The quasiparticle band gap

In the N-particle many-body neutral system, eigenstates and total energies are denoted $|\psi\rangle$ and E^N, respectively. The electron quasiparticle (QP) energies are defined by

$$\varepsilon_{ck}^{QP} = E^{N+1} - E_0^N \qquad \text{(unoccupied)} \qquad (2.1)$$

and the hole QP energies are defined by

$$\varepsilon_{vk}^{QP} = E_0^N - E^{N-1} \qquad \text{(occupied)} \qquad (2.2)$$

These are excitation energies of the $(N \pm 1)$-particle system relative to the N-particle ground-state energy E_0^N and thus correspond to the electron addition and removal energies. It is clear that $\varepsilon_{ck}^{QP} > \varepsilon_F$ and $\varepsilon_{vk}^{QP} \leqslant \varepsilon_F$, where ε_F is the Fermi level. The quasiparticle energy gap is given by

$$E_{gap} = \varepsilon_{\{CBM\}}^{QP} - \varepsilon_{[VBM]}^{QP} = E^{N+1} + E^{N-1} - 2E_0^N \qquad (2.3)$$

where ... and [...] indicate the energetically minimum and maximum **k** points of ..., and, at each **k** point, the CBM and VBM refer to the conduction band minimum and the valence band maximum, respectively.

2.2   The Green function

The propagation of one particle through the system is described by the one particle Green function. The one particle Green function is defined as:

$$G(\mathbf{x}_1,t_1,\mathbf{x}_2,t_2) = i\left\langle \Psi_N \left| T\left[\psi(\mathbf{x}_1,t_1)\psi^\dagger(\mathbf{x}_2,t_2)\right] \right| \Psi_N \right\rangle \tag{2.4}$$

It contains the information on energy and lifetimes of the quasiparticle, and also on the ground state energy of the system and the momentum distribution. Here, $x = (\mathbf{x},t) = (\mathbf{r},\sigma,t)$. Ψ_N is the Heisenberg ground state vector of the interacting N-electron system satisfying the engenvalue equation $H|\Psi_N\rangle = E|\Psi_N\rangle, \psi_H$ and $\psi_H^\dagger$ are respectively the annihilation and creation field operator and T is the Wick time ordering operator.

$$\psi(\mathbf{x},t) = e^{iHt}\psi(\mathbf{x})e^{-iHt} \tag{2.5}$$

$$\psi^\dagger(\mathbf{x},t) = e^{-iHt}\psi^\dagger(\mathbf{x})e^{iHt} \tag{2.6}$$

and the field operator satisfy the anti-commutation relation:

$$\left\{\psi(\mathbf{x}),\psi^\dagger(\mathbf{x}')\right\} = \delta(\mathbf{x}-\mathbf{x}') \tag{2.7}$$

$$\left\{\psi(\mathbf{x}),\psi(\mathbf{x}')\right\} = \left\{\psi^\dagger(\mathbf{x}),\psi^\dagger(\mathbf{x}')\right\} = 0 \tag{2.8}$$

and:

$$T[\psi(\mathbf{x}_1,t_1)\psi^\dagger(\mathbf{x}_2,t_2)] = \begin{cases} \psi(\mathbf{x}_1,t_1)\psi^\dagger(\mathbf{x}_2,t_2) & \text{if } t_1 > t_2 \\ \psi(\mathbf{x}_2,t_2)\psi^\dagger(\mathbf{x}_1,t_1) & \text{if } t_1 < t_2 \end{cases} \tag{2.9}$$

Therefore, the Green function describes the probability amplitude for the propagation of an electron (hole) from position $\mathbf{r}_2$ at t_2 to $\mathbf{r}_1$ at time t_1 for $t_1 > t_2$ ($t_1 < t_2$) (See Fig.2.1). Insert a complete set of N+1 and N-1 particle states, $\sum_j |\psi_j^{N\pm1}\rangle\langle\psi_j^{N\pm1}| = 1$, we perform a Fourier transform in energy space we obtain:

$$G(\mathbf{x}_1,\mathbf{x}_2;\omega) = \sum_s \frac{f_s(\mathbf{x}_1 f_s^*(\mathbf{x}_2)}{\omega - \varepsilon_s + i\eta\, sgn(\varepsilon_s - \varepsilon_F)} \tag{2.10}$$

$$t_1 > t_2 \qquad\qquad\qquad t_1 < t_2$$

$$\langle \Psi_0^N | \hat{\psi}(\mathbf{r_1}, t_1)\hat{\psi}^\dagger(\mathbf{r_2}, t_2) | \Psi_0^N \rangle \quad -\langle \Psi_0^N | \hat{\psi}^\dagger(\mathbf{r_2}, t_2)\hat{\psi}(\mathbf{r_1}, t_1) | \Psi_0^N \rangle$$

(a) add an electron   (b) remove an electron
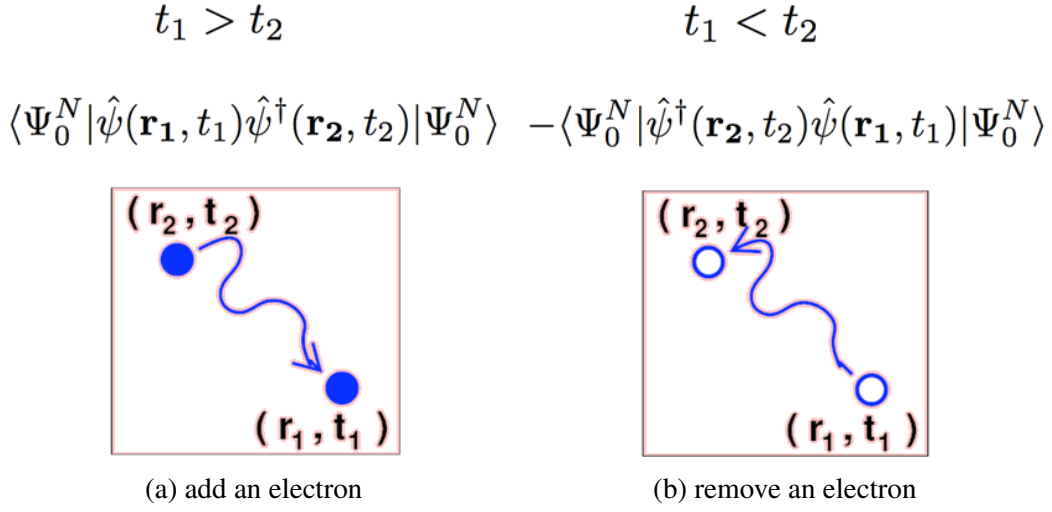
Fig. 2.1 Add/Remove an electron in the N-particle many-body system

where ε_F is the Fermi level,

$$\varepsilon_s = \begin{cases} E_s^{(N+1)} - E_N^{(N)} & \text{for } \varepsilon_s \geq \varepsilon_F \\ E_N^{(N-1)} - E_s^{(N-1)} & \text{for } \varepsilon_s < \varepsilon_F \end{cases} \tag{2.11}$$

The subscript s indicate the quantum label of the states of the $N \pm 1$ system. The amplitudes $f_s(\mathbf{x})$ are defined as:

$$f_s(\mathbf{x}) = \begin{cases} \langle \Psi_N | \psi(\mathbf{x}) | \Psi_{N+1,s} \rangle & \text{for } \varepsilon_s \geq \varepsilon_F \\ \langle \Psi_{N-1,s} | \psi(\mathbf{x}) | \Psi_N \rangle & \text{for } \varepsilon_s < \varepsilon_F \end{cases} \tag{2.12}$$

The Green function has the poles at the electron addition (removal) energies and describes quasiparticles. So we can obtain the quasiparticle band gap information from Green function.

2.3 The self-energy

From the definition of Green function (G) and the equation of motion for $\psi(\mathbf{r},t)$: $i\frac{\partial}{\partial t}\psi(\mathbf{r},t) = [\psi(\mathbf{r},t), H]$. we can show:

$$i\frac{\partial}{\partial t_1}G(1,2) = \delta(1,2) + H_0(1)G(1,2) - i\int v(1^+,3)G(1,3,2,3^+)d3 \tag{2.13}$$

Here, $H_0 = T + V_{ext} + V_H$, the number n stands for $(\mathbf{r_n}, t_n)$, $v(1^+,3)$ is the Coulomb interaction between electrons. There exists 2-particle Green function, describes the motion of 2 particles:

$$G(1,2,3,4) = - \left\langle \Psi_0^N \left| T \left[\psi(1)\psi(2)\psi^\dagger(4)\psi^\dagger(3) \right] \right| \Psi_0^N \right\rangle \tag{2.14}$$

In frequency Fourier space:

$$[\omega - H_0] G(\omega) + i \int v G_2(\omega) = 1 \tag{2.15}$$

Instead of introducing a 2-particles Green function, we introduce the self-energy operator, Σ. The self-energy allows to close formally the hierarchy of equations of motion of higher order Green functions. Equation (2.15) is tranformed to 1-particle Green function.

$$[\omega - H_0] G(\omega) + i \int \Sigma(\omega) G(\omega) = 1 \tag{2.16}$$

The self-energy is a non-local and energy dependent operator. From the equation of motion:

$$[\hbar\omega - H_0(\mathbf{r})] G(\mathbf{r},\mathbf{r}';\omega) - \int \Sigma(\mathbf{r},\mathbf{r}'';\omega) G(\mathbf{r}'',\mathbf{r}';\omega) d^3\mathbf{r}'' = \delta(\mathbf{r}-\mathbf{r}') \tag{2.17}$$

Introducing the Lehmann representation for G. The QP energies and QP wave functions can be obtained as solutions of a Schrödinger-type QP equation [40]

$$H_o \psi_{nk}(\mathbf{r}) + \int d\mathbf{r}' \Sigma(\mathbf{r},\mathbf{r}';\varepsilon_{nk}^{QP}) \psi_{nk}(\mathbf{r}') = \varepsilon_{nk}^{QP} \psi_{nk}(\mathbf{r}) \tag{2.18}$$

A practical approximation to calculate Σ is the *GW* approximation proposed by Hedin [17], who wrote the self-energy as

$$\Sigma_{GW}(\mathbf{r},\mathbf{r}';E) = \frac{i}{2\pi} \int d\omega e^{-i0^+\omega} G(\mathbf{r},\mathbf{r}';E-\omega) W(\mathbf{r},\mathbf{r}';\omega) \tag{2.19}$$

The *GW* self-energy can be separated into two terms ($\Sigma_{GW} = \Sigma x + \Sigma_c$). The exchange part is given by

$$\Sigma_x(\mathbf{r},\mathbf{r}') = \frac{i}{2\pi} \int d\omega e^{i\omega 0^+} G(\mathbf{r},\mathbf{r}';\omega) v(\mathbf{r}-\mathbf{r}') = -\sum_{n\mathbf{k}}^{occ} \frac{\psi_{n\mathbf{k}}(\mathbf{r})\psi_{n\mathbf{k}}^*(\mathbf{r})}{|\mathbf{r}-\mathbf{r}'|} \tag{2.20}$$

and the correlation part,

$$\Sigma_c(\mathbf{r},\mathbf{r}';\omega) = \frac{i}{2\pi} \int d\omega' e^{-i\omega 0^+} G(\mathbf{r},\mathbf{r}';\omega-\omega') \left[W(\mathbf{r},\mathbf{r}';\omega') - v(\mathbf{r}-\mathbf{r}') \right] \tag{2.21}$$

In equation (2.20), the symbol *occ* in the sum means that the summation is taken over the occupied states only. $\Sigma_c(\mathbf{r},\mathbf{r}';E)$ is evaluated by using the full ω integration [41]. In Equation
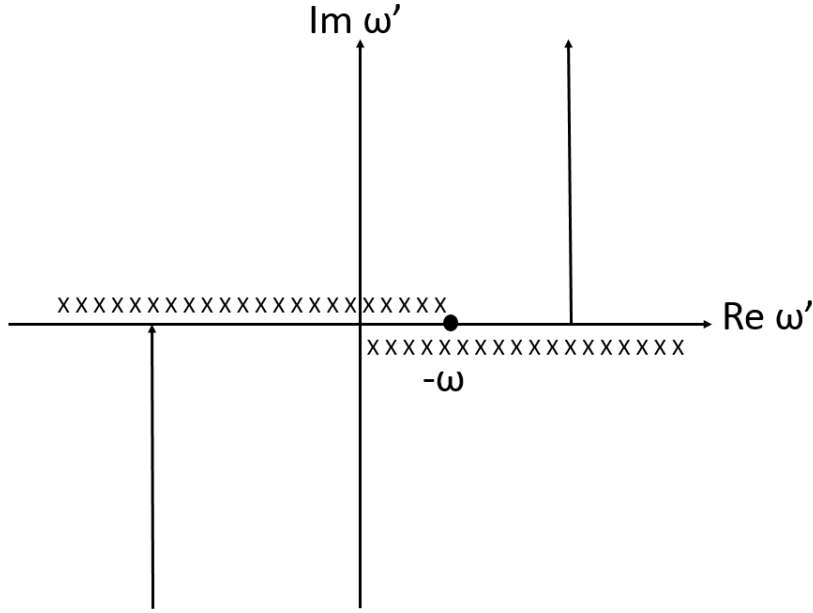
Fig. 2.2 Contour C of the ω' integration in Equation 2.22

(2.21), it is difficult to perform the ω' integral along the real axis, since W and G have a strong structure on this axis. In order to avoid this difficulty, Godby et al.[42–45] restricted the values of ω to small imaginary numbers and changed the contour of the ω' integral from real axis to imaginary axis [19]. Then, by analytic continuation, the resulting Taylor series is used to estimate the matrix elements for real values of ω. Ishii and Ohno *et al.* [41, 46] suggested that this intergration method employed by Godby *et al.* [19] can be extended rather easily to real number of ω by slightly modifying the contour. The contour along the real ω' axis from $-\infty$ to $+\infty$ for the integral Equation (2.21) can be replaced by the contour C shown in Fig.2.2 . Here we further use the symmetry $W(\omega) = W(-\omega)$ to reduce the contour to the positive real and imaginary parts only. The correlation part of self-energy's diagonal matrix element becomes

$$\langle n, \mathbf{k} | \Sigma_c(\mathbf{r}, \mathbf{r}') | n, \mathbf{k} \rangle = \sum_{n'} \sum_{\mathbf{q}} \sum_{\mathbf{G}, \mathbf{G}'} \langle n, \mathbf{k} | e^{i(\mathbf{q}+\mathbf{G})\cdot\mathbf{r}} | n', \mathbf{k}-\mathbf{q} \rangle \langle n'\mathbf{k}-\mathbf{q} | e^{-i(\mathbf{q}+\mathbf{G})\cdot\mathbf{r}} | n, \mathbf{k} \rangle$$

$$\times \frac{i}{2\pi} \int d\omega' \left[W_{\mathbf{G},\mathbf{G}'}(\mathbf{q}, \omega') - (4\pi/\Omega G^2)\delta_{\mathbf{G},\mathbf{G}'} \right]$$

$$\times (\frac{1}{\omega + \omega' - \varepsilon_{\mathbf{k}-\mathbf{q},n'} - i\delta_{\mathbf{k}-\mathbf{q},n'}} + \frac{1}{\omega - \omega' - \varepsilon_{\mathbf{k}-\mathbf{q},n'} - i\delta_{\mathbf{k}-\mathbf{q},n'}})$$

$$\tag{2.22}$$

with the help of $W(\omega) = W(-\omega)$. This term represents the contribution related to the electron correlation.

Instead of solving equation (2.18) self-consistently, we adopt here the so-called one shot *GW* approximation first proposed by Hybertsen and Louie [18]. The Green's function (*G*) is replaced by the LDA Green's function G_0 and constructed in a non-self-consistent way from the KS wave functions $\psi_{n\mathbf{k}}^{KS}(\mathbf{r})$ and eigenvalues $\varepsilon_{n\mathbf{k}}^{KS}(\mathbf{r})$. It will be discussed in the next section.

2.4   Hedin's equations

It is possible to calculate energy and lifetimes of quasiparticle excitation solving Eq. (2.18). A formally exact way of calculating the self-energy is given by a set of coupled equations, known as Hedin's equations [18]:

Self-energy:

$$\Sigma(1,2) = i \int d(34) G(1,3) \Gamma(3,2,4) W(4,1^+) \tag{2.23}$$

Screened potential:

$$W(1,2) = v(1,2) + \int d(34) v(1,3) P(3,4) W(4,2) \tag{2.24}$$

Polarization:

$$P(1,2) = -i \int d(34) G(1,3) G(4,1^+) \Gamma(3,4,2) \tag{2.25}$$

Vertex function:

$$\Gamma(1,2,3) = \delta(1,2)\delta(1,3) + \int d(4567) \frac{\partial \Sigma(1,2)}{\partial G(4,5)} G(4,6) G(7,5) \Gamma(6,7,3) \tag{2.26}$$

Dielectric function:

$$\varepsilon = 1 - vP \tag{2.27}$$

The screened potential W can also be written as

$$W(1,2) = \int d(3) \varepsilon^{-1}(1,3) v(3,2) \tag{2.28}$$

From Hedin's equations, we know how to calculate the self-energy. But it is still difficult to do in practice. So the *GW* approximation is needed.

2.5   The *GW* approximation

In *GW* approximation, the vertex function Γ in its zeroth-order form as: $\Gamma(1,2,3) = \delta(12)\delta(13)$. So the Hedin's equations become:

$$\Sigma(1,2) = iG(1,2)W(1^+,2) \tag{2.29}$$

$$G(1,2) = G_0(1,2) + \iint d(3)d(4)G_0(1,3)\Sigma(3,4)G(4,2) \tag{2.30}$$

$$P(1,2) = -iG(1,2)G(2,1) \tag{2.31}$$

$$W(1,2) = v(1,2) + \iint d(3)d(4)v(1,3)P(3,4)W(4,2) \tag{2.32}$$

Using the *GW* approximation, the quasiparticle equation (Eq. 2.18) can be solved. The quasiparticle spectrum is calculated with Eq. (2.18) using the first-order perturbation theory in ($\Sigma_{GW} - V_{xc}^{LDA}$), where V_{xc}^{LDA} is the LDA exchange-correlation potential. Usually, the KS wave functions $\psi_{n\mathbf{k}}^{KS}$ are sufficiently close to the true quasiparticle wave function $\psi_{n\mathbf{k}}(\mathbf{r})$, so that the first-order estimate of the self-energy correction to the LDA eigenvalues in adequate [18]. The *GW* quasiparticle energy $\varepsilon_{n\mathbf{k}}^{GW}$ is then obtained as

$$\varepsilon_{n\mathbf{k}}^{GW} = \varepsilon_{n\mathbf{k}}^{KS} + Z_{n\mathbf{k}} \left\langle \psi_{n\mathbf{k}}^{KS} \left| \Sigma_{GW}(\mathbf{r},\mathbf{r}';\varepsilon_{n\mathbf{k}}^{KS}) - V_{xc}^{LDA}(\mathbf{r})\delta(\mathbf{r}-\mathbf{r}') \right| \psi_{n\mathbf{k}}^{KS} \right\rangle \tag{2.33}$$

with a renormalization factor as

$$Z_{n\mathbf{k}} = \left[1 - \frac{\partial \Sigma_{GW}(E)}{\partial E} \right]^{-1}_{|E=\varepsilon_{n\mathbf{k}}^{KS}} \tag{2.34}$$

2.6   One-shot *GW* approximation

In practice, Kohn-Sham orbitals and eigenvalues from a DFT calculation are often used as input for a *GW* calculation and the quasiparticle spectrum is evaluated non-selfconsistenly from Eq.(2.33) without updating the Green's Function or the screened potential, that means only one iteration is made. This is known as the "one-shot" *GW* or G_0W_0 approximation [18, 19] and has become a standard tool in electronic structure theory. W_0 is hereby equal to the RPA screened potential.

The Scheme of the one-shot *GW* is shown in Fig.(2.3). In this thesis, electronic structures are calculated by one-shot *GW* method. Firstly, Kohn-Shan equation is solved by DFT and LDA, it obtain Kohn-Sham eigenvalues and wave fuctions. Then using one-shot *GW* approximation, we can get polarization, dielectric function, screened potential, *et. al.*. From Hedin's equations, we obtain the self-energy. Finally, we calculate the QP energy by Eq.(2.33).
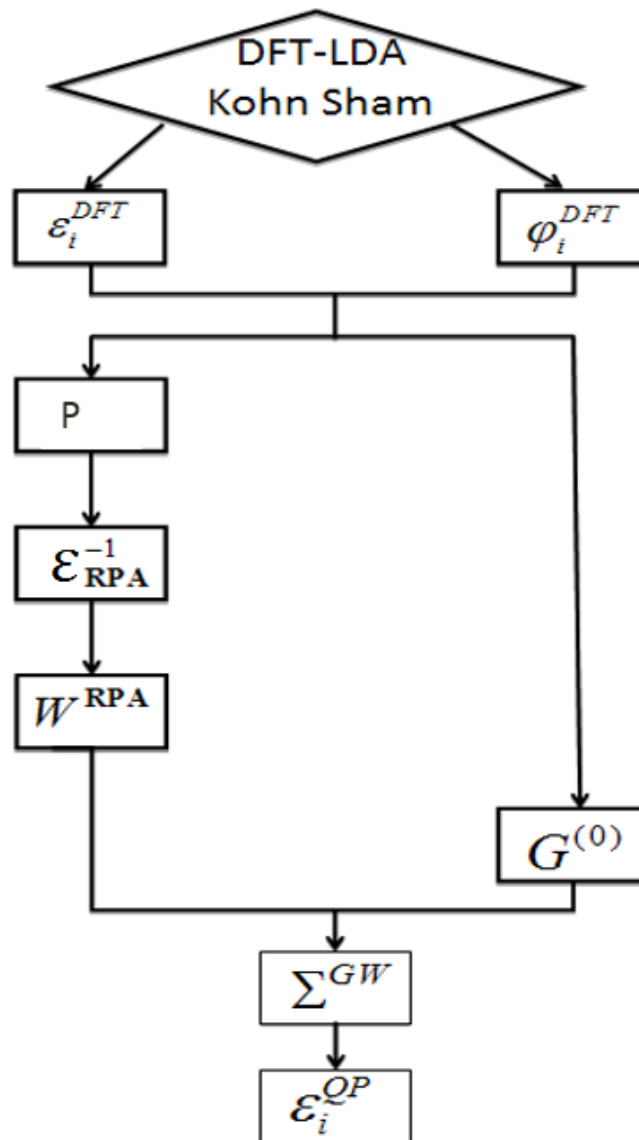
Fig. 2.3 Scheme of the one-shot *GW* calculation

Chapter 3

Computational Method

TOMBO[35, 36], all-electron mixed-basis code, is short for "TOhoku Mixed Basis Orbitals ab initio program". In this thesis, electronic structures of transition metal oxides are calculated by our original all-electron mixed basis code TOMBO developed by Prof. Kaoru Ohno, *et al.*.

3.1 Short introduction of TOMBO

Density funcitonal theroy (DFT) [10] and local density approximation (LDA) [47] have been used in numerous electronic structure calculations and firt-principles molecular dynamics (MD) simulations. To perform those calculations, Kohn–Sham (KS) equation needs to be solved self-consistently such that the input potential is identical to the output potential [47]. The electronic wave function has to be described by appropriate functions to solve the KS equation. Among the plane wave (PW) expansion approach has been applied to the ab-initio molecular dynamics (MD) simulations with reasonably high accuracy [33].

However, it is difficult to treat phenomena (hyperfine interaction, XPS, Xanes, *etc.*) related to core electrons by this method. One problem in generating good pseudo potentials is related to the fact that the core contribution to the exchangecorrelation potential is not simply an additive quantity. Moreover, it is not easy to create efficient pseudopotentials, which require only small number of plane waves.

On the other hand, linear combination of atomic orbitals (LCAO) approaches can enable us to treat all electrons. However, these methods have an intrinsic problem of incomplete basis set, and therefore there is a problem in applying them in perturbation theory or spectral expansion, which requires a description in the complete Hilbert space. It is also difficult to consider a negative affinity problem by these methods. Related but slightly different problem inherent to these methods is a basis set superposition error (BSSE) [48, 49]. There is also

some trouble in the Gaussian basis method [50] to describe cusp in the wave-funcion at the nuclear position.

In these respects, it is highly desirable to develop new method, which combines the PW expansion technique with the LCAO technique to remove pseudopotentials in the PW expansion methods and to make the basis set complete in the LCAO methods. This is the main idea to introduce the all-electron mixed basis approach. TOMBO [35, 36] is the program package using this approach. Therefore, TOMBO is the all-electron firstprinciples method, which can be applicable to both isolated and periodic systems with complete basis set. It is not the overcomplete basis set because only limited number of PWs is used in the computation.

The powerfulness of TOMBO is not only based on these features but also based on the fact that it enables us to perform the state-of-the-art calculations such as *GW* approximation and Bether–Salpeter equation. Using these methods, TOMBO can treat the problems related to electron correlations, electronic structure around the band gap, excitation spectra, and so forth.

The all-electron mixed basis approach has the following advantages:

1. The number of basis functions can be significantly reduced.

2. In Hamiltonian matrix elements, it is not necessary to store PW-PW part because it is given simply by the Fourier components $V(\mathbf{G} - \mathbf{G}')$.

3. It is possible to accurately treat core states because we determine AOs by using Herman–Skillman code with logarithmic radial mesh.

4. There is no complexity to generate and treat pseudoptentials. There is also no problem of transferability.

5. The overlap between AOs and PWs is calculated accurately by first performing angular integral analytically and then performing radial integral of spherical Bessel functions numerically in logarithmic radial mesh.

6. Because AOs are confined inside non-overlapping atomic spheres, there is no BSSE problem, and it is not necessary to calculate overlap integrals between AOs centered at different atoms, which might produce unnecessary computational errors. Simultaneously, this reduces the overcompleteness problem.

3.2   Mixed basis formulation

TOMBO is short for "TOhoku Mixed Basis Orbitals ab initio program". The "mixed-basis" indicates the method using both plane waves and Bloch sums made of atomic orbitals as the basis set.

For an isolated atom, it is possible to solves the Kohn–Sham equation very rigorously, because of the system has a spherical symmetry. In this case, the Kohn-Sham wave function is expressed as a product of radial function $R_{jnl}(r)$ and spherical harmonics $Y_{lm}(\mathbf{r})$ as

$$\phi_{jnlm}^{AO} = R_{jnl}(r)Y_{lm}(\mathbf{r}) \tag{3.1}$$

Here, j, n, l, and m are atomic species, principal quantum number, angular momentum quantum number, and magnetic quantum number.

In the mixed basis code, the KS wave function is expressed as a linear combination of PWs and AOs as follows [35]

$$\psi_v(\mathbf{r}) = \frac{1}{\sqrt{\Omega}} \sum_{\mathbf{G}} c_v^{PW}(\mathbf{G})e^{i\mathbf{G}\cdot\mathbf{r}} + \sum_j \sum_{nlm} c_v^{AO}(jnlm)\phi_{jnlm}^{AO}(\mathbf{r}-\mathbf{R}_j) \tag{3.2}$$

Here, ϕ is the volume of the unit cell, $\mathbf{G}$ is the reciprocal lattice vector, c is the expansion coefficients.

The formulation presented in the previous section based on MBPT requires summing over large number of empty states. The PW basis set can most accurately describe the empty states. In contrast, to describe the electrons in the core region accurately, the AO basis set works better then the PW basis set. The all-electron mixed basis approach, using both PWs and AOs as a basis set in a combined way, is able to meet the requirements to describe both spatially extended and localized states. In our code, AOs are numerically described inside the non-overlapping atomic spheres and the radial part is treated using the logarithmic mesh.

3.3   All-electron charge density

In the all-electron mixed basis approach, all-electron charge density $\rho(\mathbf{r})$ is made of three contributions: PW-PW, AO-PW,and AO-AO.

$$\rho(\mathbf{r}) = \rho^{PW-PW}(\mathbf{r}) + \sum_j \rho_j^{AO-PW}(\mathbf{r}) + \sum_j \rho_j^{AO-AO}(\mathbf{r}) \tag{3.3}$$

In the all-electron mixed basis approach, the charge density is made of the three contributions,

$$\rho^{PW-PW}(\mathbf{r}) = \frac{2}{\Omega} \sum_v^{occ} \sum_{\mathbf{G}} \sum_{\mathbf{G}'} c_v^{PW*}(\mathbf{G}')c_v^{PW}(\mathbf{G})e^{i(\mathbf{G}-\mathbf{G}')\cdot\mathbf{r}} \tag{3.4}$$

$$\rho_j^{AO-PW}(\mathbf{r}) = \frac{2}{\sqrt{\Omega}} \sum_v^{occ} \sum_{nlm} \sum_{\mathbf{G}} c_v^{AO*}(jnlm) c_v^{PW}(\mathbf{G}) \times \phi_{jnlm}(\mathbf{r} - \mathbf{R}_j) e^{i(\mathbf{G}) \cdot \mathbf{r}} + c.c..$$ (3.5)

$$\rho_j^{AO-AO}(\mathbf{r}) = 2 \sum_v^{occ} \sum_{n'l'm'} \sum_{nlm} c_v^{AO*}(jn'l'm') c_v^{AO}(jnlm) \times \phi_{jn'l'm'}(\mathbf{r} - \mathbf{R}_j) \phi_{jnlm}(\mathbf{r} - \mathbf{R}_j)$$ (3.6)

where c.c. in equation (3.5) means the complex conjugate of the previous term. The first PW-PW contribution can be conveniently treated in Fourier space. The rest two AO-related contributions are confined only inside the non-overlapping atomic spheres, and can be written together as

$$\rho_j^{AO}(\mathbf{r}) = \rho_j^{AO-PW}(\mathbf{r}) \rho_j^{AO-AO}(\mathbf{r})$$ (3.7)

This can be divided into two parts: one is spherical symmetric part and the other is asymmetric part.

3.4   Input parameters

In the *GW* calcualtion using TOMBO code, it needs 5 input files: INPUT.inp, COOR-DINATES.inp, KPOINT.inp, QPOINT.inp, and SPOINT.inp. INPUT.inp is the central input file of TOMBO. It determines "what to do and how to do it", and can contain a relatively large number of parameters. The variables related to both the unit cell and AOs should be written in COORDINATES.inp: the lattice constant, lattice vectors, coordinates of the nuclei and the number of orbit-type AOs for each atom.

In *GW* calculation, Self-consistent field (SCF) loop with special-point sampling (SPOINT.inp) is performed within LDA and then one-shot *GW* crystal calculation is performed. To calculate the polarization function $P_{\mathbf{GG'}}$, $\mathbf{k}$-point sampling is performed for the points in the whole Brillouin Zone (BZ) assigned as "sum" in KPOINT.inp. Then the correlation part of the self-energy, Σ_c is calculated within the full ω integration by taking $\mathbf{q}$-point sampling in the irreducible BZ by using QPOINT.inp. Finally, the expectation values of the exchange (Σ_x) and correlation (Σ_c) parts of the self-energy are evaluated for the $\mathbf{k}$ points (typically at symmetry points in the irreducible BZ) assigned as "out" in KPOINT.inp.

Chapter 4

Electronic Structure of anatase TiO$_2$ and zincblende ZnO

4.1 Computational details

(a) anatase TiO$_2$ (b) 1st BZ of anatase TiO$_2$
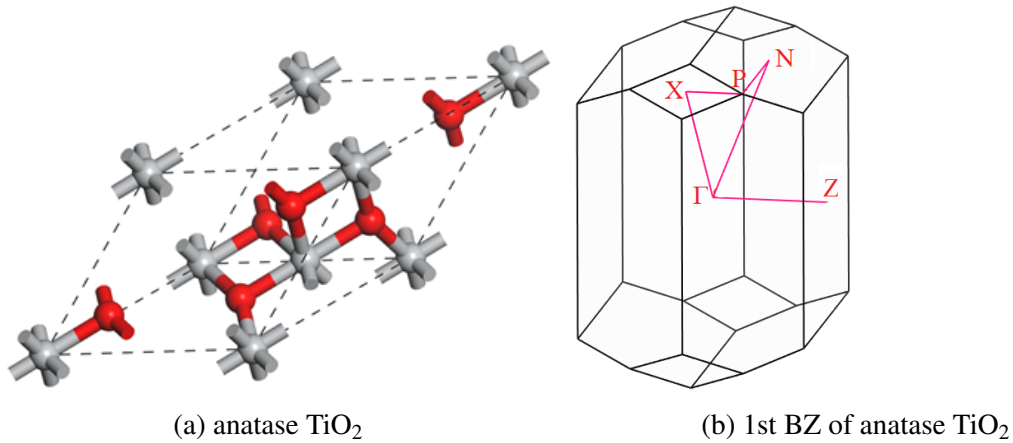
Fig. 4.1 Crystal structure and the first Brillouin zone and special **k**-points of anatase TiO$_2$. Red and gray atoms stand for oxygen and titanium atoms, respectively.

The Crystal structure, the first Brillouin zone (BZ) and special **k**-points of TiO$_2$ and ZnO are shown in Fig. (4.1) and Fig.(4.2). The *GW* calculation using TOMBO requires the following settings to ensure the convergence of QP energy: The correlation part of the self-energy, Σ_c, is calculated by performing the full ω integration using 201 points at $0.1 + 0.2n$ (eV) and $20.1 + (1 + 2n)i$ (eV) for $n = 0$, 100 along the positive real axis and then rotated $90°$ parallel to the positive imaginary axis[41] (here we utilize the relation $W(\omega) = W(-\omega)$). We use 1s, 2s and 2p valence AOs (confined within the radius of 0.65 Å)

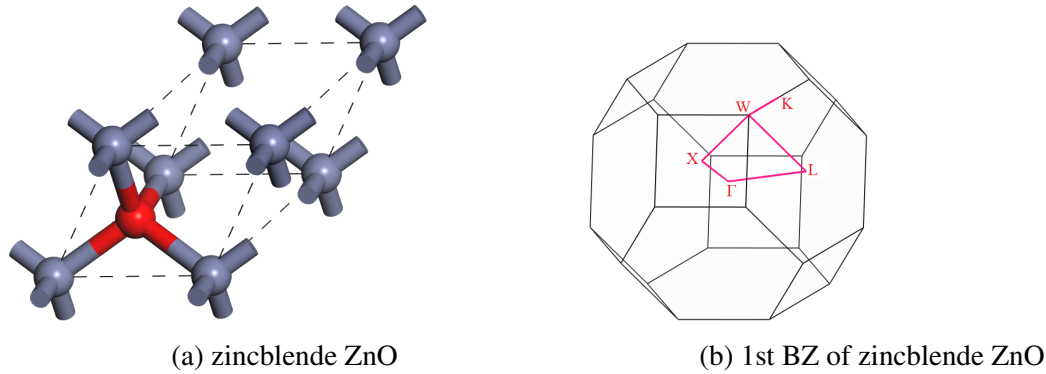(a) zincblende ZnO   (b) 1st BZ of zincblende ZnO

Fig. 4.2 Crystal structure and the first Brillouin zone and special **k**-points of zincblende ZnO. Red and black atoms stand for oxygen and zinc atoms, respectively.

for oxygen, $1s$, $2s$, $2p$, $3s$, $3p$, and $3d$ AOs (confined within the radius of 0.8 Å) for titanium and (confined within the radius of 0.85 Å) for zinc[35].

In anatase TiO_2 calculation, the cut-off energies are set as 18.29 Ry for plane waves, 73.14 for Fock exchange, and 9.33 Ry for correlation. To calculate the polarization function, **k**-point sampling is performed for the ($3\times3\times3$) points including the Γ point in the whole Brillouin zone (BZ). The number of levels used in the summation is 500. Exchange and correlation parts of the self-energy are evaluated by taking 4 **q**-points (Γ grid) sampling in the irreducible BZ.

In zincblende ZnO calculation, $3\times3\times3$ **k**-points including the Γ point are used. The cut-off energies of plane waves, Fock exchange, and correlation are set as 105.41 Ry, 421.62 Ry and 105.41 Ry , respectively. 5 **q**-points, and 1000 levels are used in zincblende ZnO calculation.

4.2   Results and discussion

Table 4.1 summarizes the band gaps of anatase TiO_2 and zincblende ZnO calculated with the LDA and *GW* methods. The band gaps of anatase TiO_2 and zincblende ZnO are 1.70 eV and 1.46 eV in the LDA calculation; the *GW* band gaps are 3.44 eV and 2.83 eV, respectively.

Comparing with the experiment data, the LDA results seriously underestimate the band gap. Due to $3d$ orbitals, there exist local electron correlations in TiO_2 and ZnO. In the LDA calculation, the band structures are not improved by the energy independent nonlocal-density corrections. Compared to the LDA results, the self-energy Σ_{GW} enlarges the band gap in the *GW* calculation, and the results are close to experiment data well.

Several band gap values of the preexisting *GW* calculations are also listed in Table 4.1. Comparing the one-shot *GW* results, there exists a quite large degree of differences.

Table 4.1 The band gaps of TiO$_2$ and ZnO calculated by LDA and GW methods (eV).

In previous GW results, values without explanation in parentheses denote the one-shot GW method, while scGW denotes the self-consistent GW method, and so on.

	LDA	present GW	previous GW	Expt.
anatase TiO$_2$	1.70	3.44	3.56[a], 3.3(GW with DFT+U)[b]	3.4 [c]
zincblende ZnO	1.46	2.83	2.12[d], 2.54(GW$_0$)[e], 3.0(GW$_0$)[f], 3.2(scGW)[g]	3.4 [h]

[a]Ref. [20]
[b]Ref. [21]
[c]Ref. [2]
[d]Ref. [27]
[e]Ref. [27]
[f]Ref. [28]
[g]Ref. [27]
[h]Ref. [9]

Table 4.2 Contributions to the quasiparticle energies of anatase TiO_2 (eV).

State	Σ_x	Σ_c	Σ_{GW}	V_{xc}^{LDA}	ε^{LDA}	ε^{GW}
CBM+1	-12.63	-4.34	-16.97	-22.56	9.86	13.57
CBM	-11.98	-3.84	-15.82	-21.23	9.10	12.88
VBM	-21.43	2.72	-18.71	-21.21	7.40	9.44
VBM-1	-21.87	2.63	-19.24	-21.72	7.37	9.36

Table 4.3 Contributions to the quasiparticle energies of zincblende ZnO (eV).

State	Σ_x	Σ_c	Σ_{GW}	V_{xc}^{LDA}	ε^{LDA}	ε^{GW}
CBM+1	-6.39	-2.89	-9.28	-13.17	21.89	24.93
CBM	-8.47	-2.73	-11.20	-13.88	9.34	11.91
VBM	-27.29	2.20	-25.09	-26.35	7.88	9.08
VBM-1	-27.62	2.44	-25.18	-26.35	7.88	9.02

In practice, Kohn-Sham orbitals and eigenvalues are used as input for a *GW* calculation. Pseudopotential or the choice of the exchange-correlation functional (including the use of DFT+U) may affect the quasiparticle energies in *GW* calculation. In our results, we used the all-electron mixed basis, and described wave functions by plane waves (PWs) and atomic orbitals (AOs), which would improve the accuracy of quasiparticle energies. Our results are certainly much closer to the experimental values.

In the *GW* calculation of anatase TiO_2 , QP energy contributions form the LDA exchange-correlation V_{xc}^{LDA}, the exchange(Σ_x) and correlation (Σ_c) parts of the self-energy Σ_{GW} are listed in Table 4.2. The values of the LDA exchange-correlation V_{xc}^{LDA} in CBM and VBM are very close (-21.23 eV in CBM, and -21.21 eV in VBM). The self-energy Σ_{GW} values of anatase TiO_2 is -15.82 eV in the CBM; this value becomes -18.71 in the VBM. The difference $\Sigma_{GW} - V_{xc}^{LDA}$ becomes relatively larger from the VBM to the CBM. Consequently the *GW* method increases the gap between the valence and conduction states, and improves the underestimated LDA results.

Table 4.3 lists QP energy contributions in the *GW* calculation of zincblende ZnO. The LDA results also underestimate the band gap, the *GW* approximation enlarges the band gap, resulting in better results. The Σ_x value of zincblende ZnO in the CBM is -8.47 eV. Comparing with Table 4.2 , the Σ_x value of anatase TiO_2 in the CBM is -11.98 eV. The Σ_x absolute values of ZnO in the CBM are much smaller than that of TiO_2. From Eq. (2.20), the

Σ_x value is estimated with the following equation:

$$\langle \psi_{n\mathbf{k}} | \Sigma_x(\mathbf{r},\mathbf{r}') | \psi_{n\mathbf{k}} \rangle = -\sum_{n'\mathbf{k}'}^{occ} \iint \frac{\psi_{n\mathbf{k}}^*(\mathbf{r})\psi_{n'\mathbf{k}'}(\mathbf{r})\psi_{n'\mathbf{k}'}^*(\mathbf{r}')\psi_{n\mathbf{k}}(\mathbf{r}')}{|\mathbf{r}-\mathbf{r}'|} d\mathbf{r}d\mathbf{r}'. \qquad (4.1)$$

Since the summation runs over the occupied states only, if $|\psi_{n\mathbf{k}}\rangle$ is an occupied state, the Σ_x value becomes large negative; On the other hand, if $|\psi_{n\mathbf{k}}\rangle$ is an empty state, there is no large overlap between $\psi_{n\mathbf{k}}$ and $\psi_{n'\mathbf{k}'}$, leading to a small negative value of Σ_x. The correlation part Σ_c of the self-energy has an opposite tendency against this exchange part Σ_x, reflecting the effect of the electron screening.

There is much less overlap of ZnO than that of TiO_2 with the unoccupied states in the CBM. This is because the electron configuration is $1s^2 2s^2 2p^6 3s^2 3p^6 3d^2 4s^2$ for Ti atom and $1s^2 2s^2 2p^6 3s^2 3p^6 3d^{10} 4s^2$ for Zn atom, and $3d$ orbitals are fully occupied in Zn atom but not in Ti atom.

4.3   Conclusions

The quasiparticle band structure of anatase TiO_2 and zincblende ZnO were calculated using the all-electron mixed basis GW method. The LDA gives too small band gap. In the GW calculation, the difference $\Sigma_{GW} - V_{xc}^{LDA}$ in the CBM becomes larger than that in the VBM, which leads to a large change of quasiparticle energy between the VBM and CBM. Consequently the GW method increases the gap between the valence and conduction states, and improves the underestimated LDA results. By comparing the electronic structure calculated by DFT or other GW methods, our results of the electronic structure calculation using the one-shot GW approximation with the all-electron mixed basis approach, in anatase TiO_2 case, the results are in reasonable agreement with experiments. The present GW method may help understanding the electronic structure of not heavily correlated transition metal oxides.

Chapter 5

Electronic Structure of rutile TiO$_2$ with and without Nb impurities

It has been also reported with much interest that Nb impurities affect the conductivity and optical properties of rutile TiO$_2$ [11, 12]. It is therefore highly desirable to present a systematic theoretical explanation of their electronic structures. The band gap calculated by the LDA is less than 0 eV, which conflicts with the experimental observation [51]. The *GW* method corrects the band structure well. In this chapter, the electronic structures of both pure rutile TiO$_2$ and Ti$_{1-x}$Nb$_x$O$_2$ are calculated by the *GW* method.

5.1   Computational details

Rutile TiO$_2$ has a tetragonal primitive cell with two formula units [see Fig. 5.1(a)] and its symmetry is described by the space group P42/mnm. The lattice parameters are $a = b = 4.594$Å and $c = 2.959$Å at room temperature. The Ti and O atoms reside at the 2a and 4f Wyckoff positions, the latter characterized by the single internal parameter $u = 0.305$.[52] The first Brillouin zone (BZ) of rutile TiO$_2$ is shown in Fig. 5.1(b).

In the *GW* calculation of TiO$_2$ with impurities, a larger supercell improves the accuracy of the results. However because the *GW* calculation is very heavy and there is a limitation in the computational resources, we have to use a rather small supercell.

FIG. 3(a) of Ref. [12] clearly shows the occupied impurity band about 1.3 eV below the conduction band and the location of this impurity level does not significantly depend on the impurity concentration (See Fig. 5.2). Moreover, there is no ESR signal in the Nb doped TiO$_2$ samples, which indicates that the there is no unpaired electron localized at the Nb impurity atom. From these experimental observations, we have noticed that Nb impurity
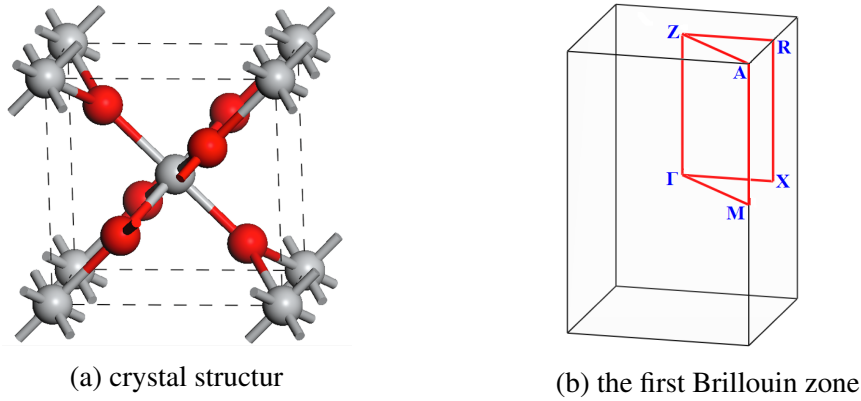
(a) crystal structur

(b) the first Brillouin zone

Fig. 5.1 The crystal structure (a) and the first Brillouin zone (b) including symmetry **k** points of rutile TiO_2. Red and gray atoms stand for oxygen and titanium atoms, respectively.

Table 5.1 Total energy of $Ti_{0.75}Nb_{0.25}O_2$ at different position

Position	Total energy (eV)
A(0.75, 0.75, 0.5)	-236.32
B(0.5, 0.5 ,0)	-235.98
C(0.25, 0.75, 0.5)	-236.20
D(0, 0.5, 0)	-235.80

atom (which has odd number of electrons) does not show spin magnetic moment. In order to realize these experimental situations, Nb impurity chain is assumed instead of an isolated Nb impurity atom, which suppresses the local spin magnetic moment. In our model, we consider a relatively high impurity concentration. Ion channeling experiments suggest that Nb atom substitutes a Ti site [51]. Therefore, we use a $2 \times 2 \times 1$ supercell, and two Ti atoms are replaced by two Nb atoms.

To determine the impurity position of Nb atom, we compared total energies of the four possible positions [(0.75, 0.75, 0.5), (0.5, 0.5, 0), (0.25, 0.75, 0.5), and (0, 0.5, 0)] of one Nb atom with the other Nb atom fixed at the position (0.25, 0.25, 0.5); see Fig. 5.3. The atomic positions are optimized by the geometric optimization using the VASP (PAW) code,[53, 54] which is converged when all forces are smaller than 10^{-3} eV/Å and allowed 10^{-6} eV error in the total energy using an LDA approach, the plane-wave cut-off energy is set as 350 eV, and a **k**-point grid of $3 \times 3 \times 8$ is used for BZ integrations.

As seen from Table 5.1, when the Nb atom substitutes the Ti atom at the position (0.75, 0.75, 0.5), the total energy is the lowest, and the crystal structure is most stable. The lattice parameters are slightly changed, $a = b = 9.12$Å, $c = 2.92$Å; $\alpha = \beta = 90°$, $\gamma = 89.56°$. So,
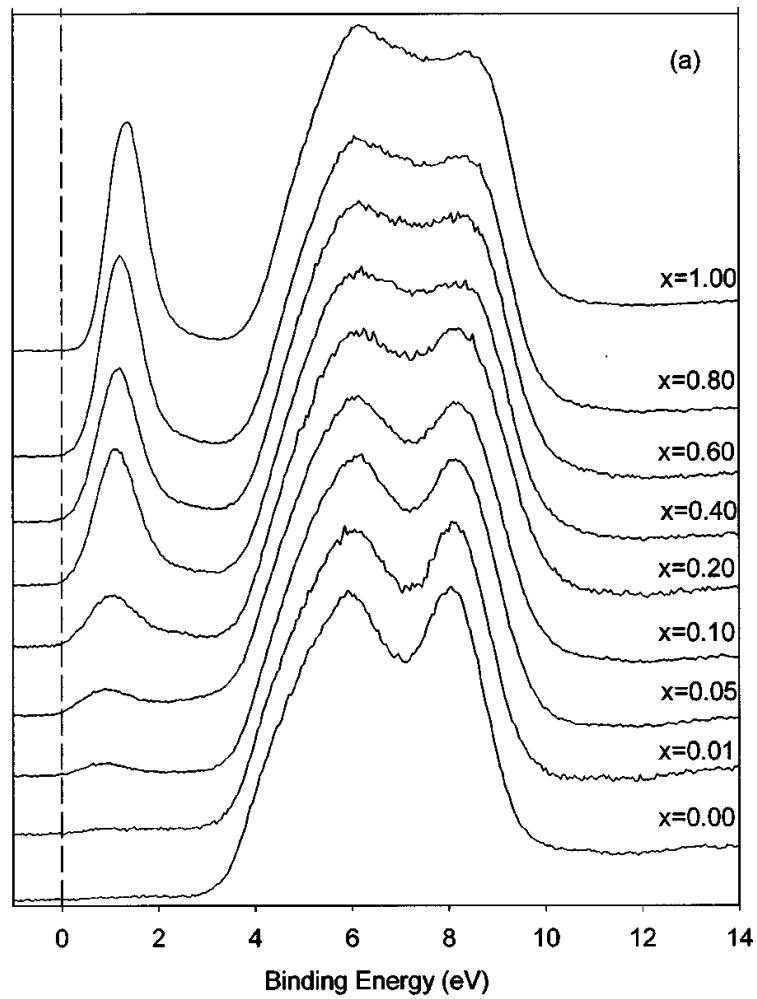
Fig. 5.2 Valence-band x-ray photoemission spectra of $Ti_{1-x}Nb_xO_2$ ceramics for the differing x values indicated. Binding energies are relative to the Fermi energy of a calibrant silver foil. [This figure is taken from D. Morris et al., Phys. Rev. B **61**, 13445 (2000).]
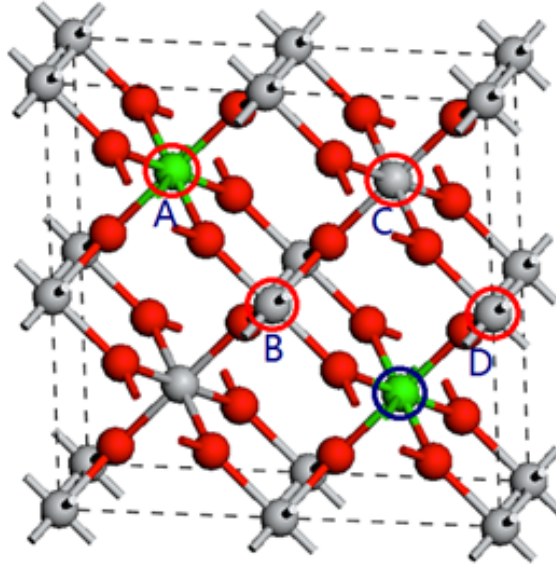
Fig. 5.3 Crystal structure of $Ti_{0.75}Nb_{0.25}O_2$. Red, gray, and green atoms stand for oxygen, titanium and niobium atoms, respectively.

we performed the *GW* calculation using Fig. 5.4(a) structural model. Its first BZ is shown in Fig. 5.4(b).

The *GW* calculation using TOMBO requires the following settings to ensure the convergence of QP energy: The correlation part of the self-energy, Σ_c, is calculated by performing the full ω integration using 201 points at $0.1 + 0.2n$ (eV) and $20.1 + (1 + 2n)i$ (eV) for $n = 0$, 100 along the positive real axis and then rotated 90° parallel to the positive imaginary axis[41] (here we utilize the relation $W(\omega) = W(-\omega)$). We use $1s$, $2s$ and $2p$ valence AOs (confined within the radius of 0.65 Å) for oxygen, $1s$, $2s$, $2p$, $3s$, $3p$, and $3d$ AOs (confined within the radius of 0.8 Å) for titanium, and $1s$, $2s$, $2p$, $3s$, $3p$, $3d$, $4s$, $4p$, $4d$ AOs (confined within the radius of 1.0 Å) for niobium[35]. For rutile TiO_2, the cut-off energies are set as 33.58 Ry for PWs, 170.01 Ry for Fock exchange, and 13.12 Ry for correlation. To calculate the polarization function, **k**-point sampling is performed in the Γ grid ($3 \times 3 \times 5$) in the whole BZ, while we used 6 **q**-points in the irreducible BZ, although we found that $3 \times 3 \times 5$ **k**-points and $3 \times 3 \times 3$ **k**-points give only 0.03 eV difference in the resulting absolute QP energies. The number of levels used in the summation is 400. For $Ti_{0.75}Nb_{0.25}O_2$, the cut-off energies are set as 13.28 Ry for PWs, 34.01 Ry for Fock exchange, and 13.28 Ry for correlation. The Γ grid $3 \times 3 \times 3$ **k**-points, 1 **q**-point, and 400 levels are used; leading to a convergence of the absolute QP energy to about 0.02 eV.

(a)   (b)
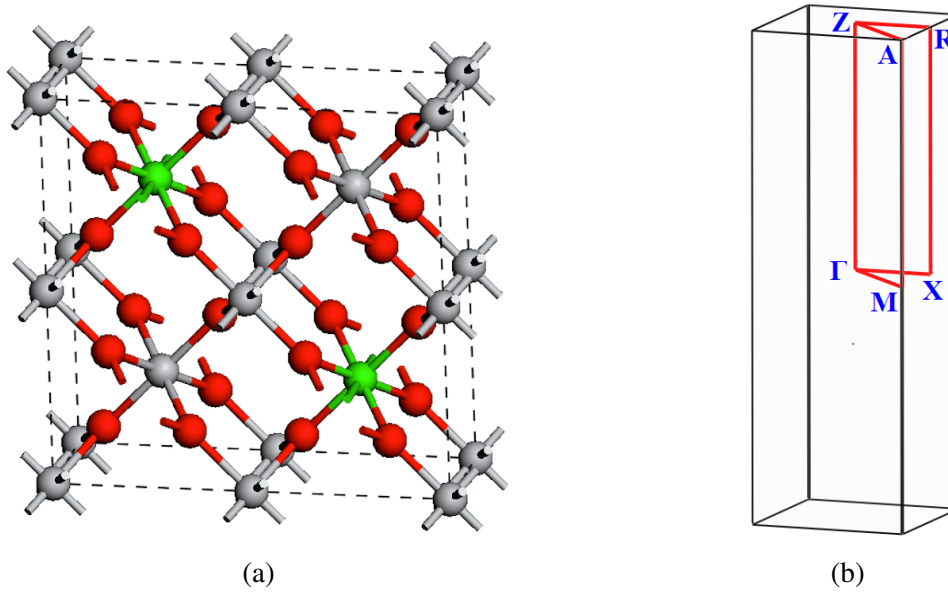
Fig. 5.4 The crystal structure (a) and the first Brillouin zone (b) including symmetry **k** points of $Ti_{0.75}Nb_{0.25}O_2$. Red, gray, and green atoms stand for oxygen, titanium and niobium atoms, respectively.

5.2   Results and discussion

5.2.1   Pure rutile TiO_2

We first performed calculations for pure rutile TiO_2. The resulting *GW* and LDA band structures are shown in Fig. 5.5. The zero of energy is placed at the [VBM]. As anticipated, LDA predicts too small band gap. The values of the energy gap calculated by the LDA and *GW* methods are 1.68 eV and 3.30 eV, respectively. The top of the valence band [VBM] is located at the Γ point and the bottom of the conduction band CBM is located at the R point. Compared to the LDA band structure, the self-energy Σ_{GW} enlarges the band gap in the *GW* band structure. The indirect band gap between the Γ and R points of 3.30 eV accords with the experiment data $(3.3 \pm 0.5$ eV)[5] well. Although some of previous reports of the *GW* calculations have referred to the experimental value 3.05 eV,[3, 55] this value is the optical gap including the excitonic effect and not the true energy gap defined by Eqs. (2.1)-(2.3). The experimental band width below the VBM[12] is about 6 eV, and our *GW* band width is 5.7 eV, which are also comparable each other.

There have been several *GW* calculations reported for the band gap of the pure rutile TiO_2 as listed in Table 5.2. Oshikiri *et al.*[22] used LMTO-ASA based one-shot *GW* calculation to obtain about 4.8 eV for the band gap. Schilfgaarde, Kotani *et al.*[24, 25] performed

Table 5.2 The band gap of rutile TiO_2 calculated by *GW* methods (eV).

Band gap	Calculation methods	References
3.30	one-shot *GW*	this work
4.8	one-shot *GW*	Ref. [22]
3.78	self-consistent *GW*	Refs. [24, 25]
3.59	one-shot *GW*	Ref. [23]
3.34	one-shot *GW*	Ref. [20]
4.48	*GW* with GGA+*U*	Ref. [26]
3.3 ± 0.5	Experiment	Ref. [5]
3.6 ± 0.2	Experiment	Ref. [6]

full-potential LMTO based self-consistent *GW* calculation and obtained 3.78 eV for the band gap. Chiodo et al.[23] reported 3.59 eV by using the plane-wave based QUANTUM-ESPRESSO. Kang and Hybertsen[20] reported the Γ-R indirect band gap of 3.34 eV by using the plane-wave based one-shot *GW* code, pointing out that the use of the GPP model of Hybertsen-Louie[18] overestimates the band gap by 0.6 eV compared to the results using the full ω integration or the plasmon-pole model (PPM) of von der Linden–Horsch.[3] In our all-electron mixed basis code, we found a similar energy gap difference of 0.7 eV between the GPP model and the PPM of von der Linden–Horsch [56](or the full ω integration). This is due to the complex structure in the loss function, i.e. $-\mathrm{Im}\varepsilon^{-1}$, in the TiO_2 crystal, which makes difficult to apply the PPMs, as discussed in Ref. [20]. More recently Lany[26] used the *GW* calculation with self-consistent quasiparticle energies but with fixed GGA +*U* wave function using VASP and obtained 4.48 eV for the band gap. They also gave TDDFT-based local-field corrected values of 3.11 eV and 3.4 eV by introducing empirical d-orbital on-site energy. These values of the *GW* band gap are very scattered, but our all-electron one-shot *GW* result of 3.30 eV using the full ω integration is close to the result of Kang and Hybertsen[20].

In the *GW* calculation, QP energy contributions from the LDA exchange-correlation potential, $V_{\mathrm{xc}}^{\mathrm{LDA}}$, and the exchange ($\Sigma_{\mathrm{x}}$) and correlation ($\Sigma_{\mathrm{c}}$) parts of the self-energy Σ_{GW} are listed in Table 5.3. We focus on the band energies of the VBM and CBM. As will be seen in Section 5.2.3, the VBM is composed of O 2*p* and Ti 3*d* orbitals, and the CBM is mainly composed of Ti 3*d* orbitals. The difference $\Sigma_{GW} - V_{\mathrm{xc}}^{\mathrm{LDA}}$ is relatively small at the Γ (2.28 eV) and R (2.11 eV) points in the VBM. Consequently the change in the energy between the LDA and *GW* calculations, ΔV_{VBM}, is less than 1.7 eV. One the other hand, the difference $\Sigma_{GW} - V_{\mathrm{xc}}^{\mathrm{LDA}}$ is rather large at the Γ (4.36 eV) and R (4.11 eV) points in the CBM, which leads to a large change in ΔV_{CBM}. Consequently the *GW* method increases the gap between the valence and conduction states, and improves the underestimated LDA results.

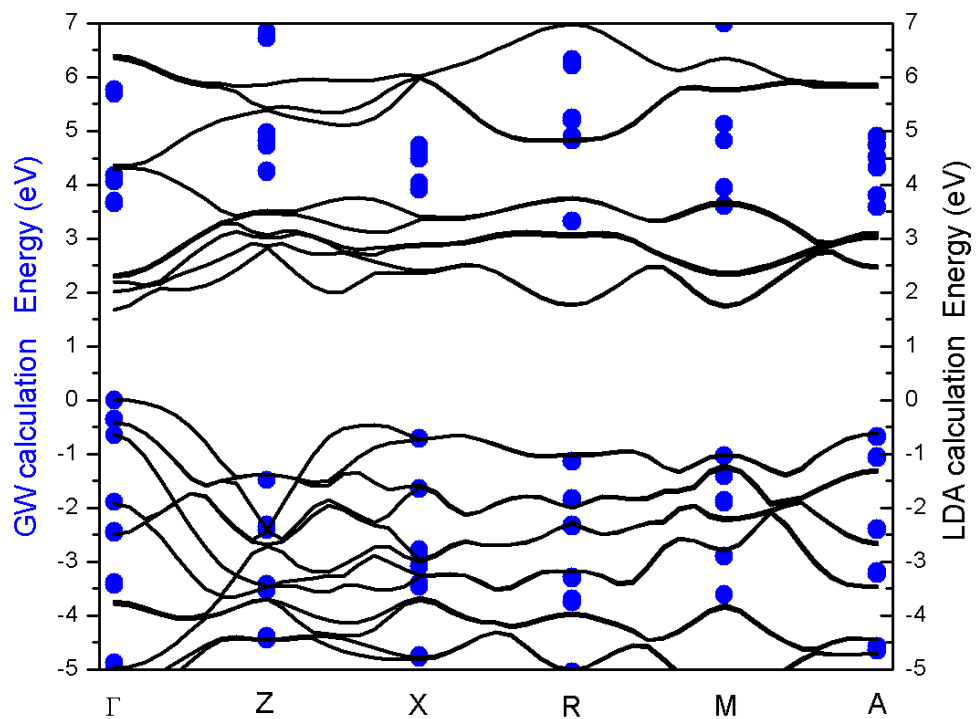Fig. 5.5 Band structure of the pure rutile TiO$_2$. (Lines for the LDA, dots for the *GW* calculation. The zero of energy is placed at the top of the valence band ([VBM] at the Γ point).

Table 5.3 Contributions to the quasiparticle energies of rutile TiO_2 at the Γ and R points.

The expectation values of the exchange (Σ_x) and correlation (Σ_c) parts of the self-energy Σ_{GW}, and the LDA exchange-correlation potential V_{xc}^{LDA} are listed together with the Kohn-Sham energy eigenvalues $\varepsilon_{n\mathbf{k}}^{KS}$ and the *GW* quasiparticle energies $\varepsilon_{n\mathbf{k}}^{GW}$ (in units of eV). The top of the valence band and the bottom of the conduction band are denoted by [VBM] (at the Γ point) and CBM (at the R point), respectively.

	state	Σ_x	Σ_c	Σ_{GW}	V_{xc}^{LDA}	$\varepsilon_{n\mathbf{k}}^{KS}$	$\varepsilon_{n\mathbf{k}}^{QP}$
Γ	CBM+1	−13.31	−4.46	−17.77	−21.99	10.78	14.17
	CBM	−13.06	−4.93	−17.99	−22.35	10.44	14.12
	[VBM]	−22.21	2.91	−19.30	−21.58	8.76	10.48
	VBM−1	−22.38	2.74	−19.64	−21.83	8.36	10.10
R	CBM+1	−13.13	−4.64	−17.77	−21.89	10.54	13.80
	{CBM}	−13.16	−4.63	−17.79	−21.90	10.52	13.78
	VBM	−21.62	3.09	−18.53	−20.64	7.76	9.34
	VBM−1	−21.68	3.14	−18.54	−20.67	7.73	9.32

The reason of this difference between the VBM and CBM is related to the difference between the occupied and unoccupied states. In this sense, the CBM and CBM+1 have a similar tendency, while the VBM and VBM−1 have a similar tendency. The characteristic of these tendencies is explained as follows. In Table 5.3, the Σ_x (or Σ_c) values are small negative (or negative) in the empty CBM and CBM+1 levels, and large negative (or positive) in the occupied VBM and VBM−1 levels.

5.2.2 $Ti_{0.75}Nb_{0.25}O_2$

The band structure of $Ti_{0.75}Nb_{0.25}O_2$ calculated with the *GW* method is shown in Fig. 5.6. There appears a clear occupied impurity band (new VBM) in the middle of the large band gap. Comparing with the band structure of the pure rutile TiO_2 given in Fig. 5.5, the magnitude of the host band gap is almost unchanged, while, due to the emergence of the occupied impurity band, the new band gap between the top of the new valence band [VBM] at the A point and the bottom of the conduction band CBM at the X point becomes smaller. As shown in Fig. 5.6, $Ti_{0.75}Nb_{0.25}O_2$ has an indirect band gap of 1.25 eV from the A point to the X point in the *GW* calculation. In the LDA calculation, on the other hand, the KS energy eigenvalue $\varepsilon_{n\mathbf{k}}^{KS}$ of the VBM is 12.73 eV at the A point, while that of the CBM is 12.36 eV at the X point. The energy of the CBM is less than that of the VBM, and therefore the band gap calculated by the LDA is less than 0 eV, which conflicts with the experimental observation.[51] The *GW* method corrects the band structure well. Contributions to the quasiparticle energies at

the A and X points are listed in Table 5.4. The value of V_{xc}^{LDA} is almost the same between the VBM and CBM. Therefore, we have an incorrect band gap in the LDA calculation. In the *GW* calculation, because of the large self-energy contribution to the VBM and CBM energies, the band gap is enlarged, leading to the results in qualitative agreement with the experiments.[12, 51]
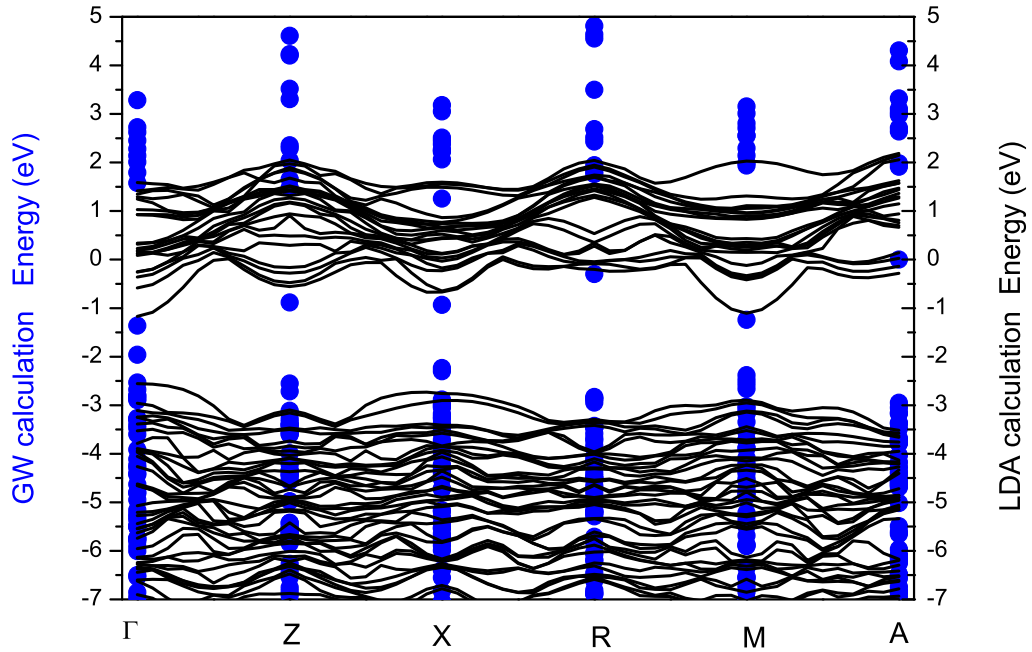

Fig. 5.6 Band structure of the $Ti_{0.75}Nb_{0.25}O_2$. (Lines for the LDA, dots for the *GW* calculation. The zero of energy is placed at the top of the valence band ([VBM] at the A point).

In order to understand how the Nb impurity affects the band structure, we discuss QP energy contributions listed in Table 5.4 by comparing with Table 5.3. The characteristic of the values of Σ_x and Σ_c is the same between the pure and with Nb impurity systems for every level except for the VBM. That is, in both tables, Σ_x and Σ_c are negative for the CBM and CBM+1; Σ_x is large negative and Σ_c is positive for the VBM−1. But the characteristic drastically changes for the VBM. With Nb impurities, it is seen from Tables 5.3 and 5.4 that Σ_c changes sign from positive to negative and Σ_x changes from large negative to small negative, i.e., their values become similar to those of the empty states, CBM and CBM+1. Again from Eq. (4.1), we find that there is only few overlap with the occupied states in the VBM, which leads to the smaller negative value for Σ_x, and Σ_c has the opposite tendency

Table 5.4 Contributions to the quasiparticle energies of $Ti_{0.75}Nb_{0.25}O_2$ at the A and X points.

The expectation values of the exchange (Σ_x) and correlation (Σ_c) parts of the self-energy Σ_{GW}, and the LDA exchange-correlation potential V_{xc}^{LDA} are listed together with the Kohn-Sham energy eigenvalues ε_{nk}^{KS} and the *GW* quasiparticle energies ε_{nk}^{GW} (in units of eV). The top of the "impurity" valence band and the bottom of the conduction band are denoted by [VBM] (at the A point) and CBM (at the X point), respectively. The band gap is positive in the *GW* approximation but negative in the LDA.

	state	Σ_x	Σ_c	Σ_{GW}	V_{xc}^{LDA}	ε_{nk}^{KS}	ε_{nk}^{QP}
A	CBM+1	−14.66	−3.47	−18.13	−22.05	13.04	15.69
	CBM	−14.17	−2.80	−16.97	−20.63	12.87	15.62
	[VBM]	−17.39	−2.70	−20.09	−21.40	12.73	13.71
	VBM−1	−22.63	3.69	−18.94	−20.49	9.49	10.66
X	CBM+1	−13.74	−4.05	−17.79	−22.25	12.78	15.92
	{CBM}	−14.15	−3.13	−17.28	−20.60	12.36	14.96
	VBM	−16.87	−3.15	−20.02	−20.58	12.34	12.77
	VBM−1	−23.32	3.91	−19.41	−21.05	10.25	11.47

(i.e., changing from positive to negative) due to the electron screening effect. This VBM is a "new" occupied impurity band caused by Nb atom, unlike the occupied states of the pure rutile TiO_2.

5.2.3   Partial charge density analysis

We show the contour plots of the partial charge density of the VBM and CBM of the pure rutile TiO_2 and the $Ti_{0.75}Nb_{0.25}O_2$ in Fig. 5.7. From Figs. 5.7 (a) and (b) of the pure rutile TiO_2, we see that the [VBM] (at the Γ point) is composed of O $2p$ and Ti $3d$ orbitals and the CBM (at the R point) is mainly composed of Ti $3d$ orbitals. The O $2p$ and Ti $3d$ orbitals play an important role in the VBM. With Nb impurities, the partial charge density of the VBM−1 (at the Γ point) is composed of O $2p$ and Ti $3d$ orbitals as seen in Fig. 5.7(c), and that of the CBM+1 (at the X point) is mainly composed of Ti $3d$ orbitals as seen in Fig. 5.7(f), which is similar to Fig. 5.7(b) of the CBM of the pure rutile TiO_2. By comparing Fig. 5.7(c) with Fig. 5.7(a), we find that the partial charge density of the VBM−1 of the $Ti_{0.75}Nb_{0.25}O_2$ is similar to that of the VBM of the pure rutile TiO_2, except that the intensity of the partial charge density in particular around some of Ti atoms of the VBM−1 of the $Ti_{0.75}Nb_{0.25}O_2$ is less than that of the VBM of the pure rutile TiO_2. (Note that all Ti atoms are on the same plane in this figure.) This is because some parts of Ti $3d$ and O $2p$ orbitals are hybridized with Nb $4d$ orbitals in the VBM. In fact, the [VBM] (at the A point) and the
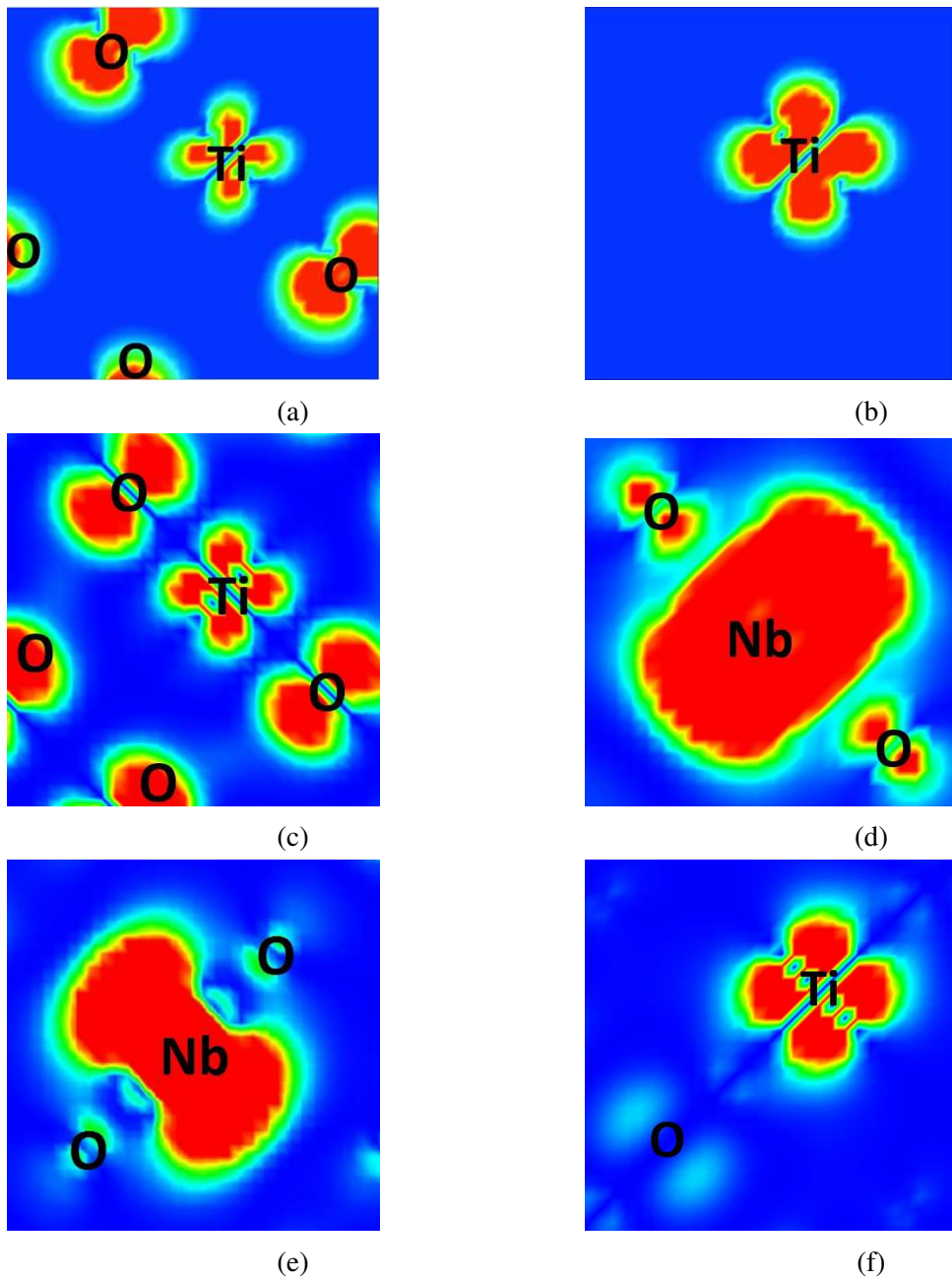
Fig. 5.7 Contour plots of the partial charge density of the VBM and CBM of the pure rutile TiO$_2$ and the Ti$_{0.75}$Nb$_{0.25}$O$_2$ on (0 0 1) plane with same magnification.
The two figures: (a) is the [VBM] (at the Γ point) and (b) is the CBM (at the R point), both for the pure rutile TiO$_2$. The four figures: (c) is the VBM-1 (at the Γ point), (d) is the [VBM] (at the A point), (e) is the CBM (at the X point), and (f) is the CBM$+1$ (at the X point), all for the Ti$_{0.75}$Nb$_{0.25}$O$_2$.

CBM (at the X point) are mainly composed of Nb $4d$ orbitals, and a few of O $2p$ and Ti $3d$ orbitals as seen in Fig. 5.7(d) and Fig. 5.7(e). It indicates that these VBM and CBM are the Nb-origin impurity level split off from the VBM-1 and CBM$+1$ (i.e., the host VBM and CBM) with Nb impurities. Thus, this occupied impurity band emerges at higher energy than the host VBM level, and unoccupied impurity band emerges at lower energy. Since the magnitude of the host band gap is almost unchanged and this impurity band is fully occupied by electrons, it reduces the band gap. From Fig. 5.7(d), we see that there is a little overlap between O $2p$ and Nb $4d$ orbitals, although O $2p$ orbitals do not much affect the VBM with Nb impurities. The previous experimental study[12] has shown that Nb introduces a deep state lying about 1.3 eV below the conduction band edge, and the new Nb $4d$ states overlap the O $2p$. Our result is in reasonable agreement with this experimental observation. Indeed, the UPS observation (Fig. 3(a) of Ref. [12]) clearly shows the impurity band about 1.3 eV below the conduction band and the location of this impurity level does not significantly depend on the impurity concentration. Moreover, there is no ESR signal in the Nb doped TiO$_2$ samples, which indicates that there is no unpaired electron localized at the Nb impurity atom. From these experimental observations, we have noticed that Nb impurity atom (which has odd number of electrons) does not show spin magnetic moment. Therefore we think that our model is reasonable to realize these experimental situations in real TiO$_2$ samples in a sense that Nb impurity chain instead of an isolated Nb impurity atom suppresses the local spin magnetic moment and the relatively high impurity concentration would also correspond to the UPS data mentioned above.

5.3   Conclusion

In this paper, we have discussed the quasiparticle band structure of the pure rutile TiO$_2$ and Ti$_{0.75}$Nb$_{0.25}$O$_2$ using the *GW* approximation. The *GW* method increases the energy gap between the valence and conduction states, and corrects the underestimated results of the LDA. In particular, in the case with Nb impurities, the *GW* results open up the zero gap of the LDA. The top of the valence band ([VBM]) at the Γ point of the pure rutile TiO$_2$ is composed of O $2p$ and Ti $3d$ orbitals, and the bottom of the conduction band (CBM) at the R point is mainly composed of Ti $3d$ orbitals. With Nb impurities, a new occupied impurity band appears in the middle of the host band gap as the new VBM. Therefore, the energy level of VBM increases and the energy gap decreases (but still finite), because the host levels do not change much. The behavior of the exchange and correlation contributions to the self-energy is clearly changed in the VBM. The VBM of the Ti$_{0.75}$Nb$_{0.25}$O$_2$ is composed of Nb $4d$ orbitals, a few of O $2p$ and Ti $3d$ orbitals. The CBM$+1$ and VBM-1 of Ti$_{0.75}$Nb$_{0.25}$O$_2$ are

similar to the CBM and VBM of the pure rutile TiO_2, respectively. The occupied impurity band produced by the Nb impurity atoms certainly reduces the band gap, which increases electronic conductivity and improves thermoelectric properties. Our results of the electronic structure are in reasonable agreement with experiments. Our method may help understanding the change in the electronic structure of not so strongly correlated transition metal oxide with impurities.

Chapter 6

Conclusions and Outlook

6.1 Conclusions

Transition metal oxides have unusual and useful electronic properties, because of open d and f electron shells,and are used in wide variety of applications. It is important to study electronic structures of doped transition metal oxides in order to understand the physics of material properties. Band gap calculated by DFT is usually underestimated by 30-50%. To achieve accurate electronic structure, electronic structures are calculated by GW approximation using TOMBO code.

In this thesis, I calculated the band structure of znic oxide and titanium dioxide using GW approximation, and studied the physcisal mechanism of rutie TiO_2 with impurities.

Chapter 4. I calculated the electronic structure of pure TiO_2 and ZnO. Compared the LDA band structure, the self-energy enlarges the band gap in the GW band structure. In the GW calculation, the difference $\Sigma_{GW} - V_{xc}^{LDA}$ is relatively small in the VBM. Consequently the change in the energy between the LDA and GW calculations, ΔE_{VBM}, is small. One the other hand, the difference $\Sigma_{GW} - V_{xc}^{LDA}$ is rather large in the CBM, which leads to a large change in ΔE_{CBM}. Consequently the GW method increases the gap between the valence and conduction states, and improves the underestimated LDA results.

Chapter 5. With Nb impurities in rutile TiO_2, it is seen that Σ_c changes sign from positive to negative and Σ_x of the VBM becomes a small negative value from a large negative value, their values become similar to those of the empty states (CBM and CBM+1). We find that there is only few overlap with the occupied states in the VBM, which leads to the smaller negative value for Σx, and Σc has the opposite tendency (i.e., changing from positive to negative) due to the electron screening effect. This VBM is a "new" impurity level caused by Nb doping, unlike the occupied states of the pure rutile TiO_2.

In the strongly correlated transition metal oxides system, the LDA approximation gives too small band gap, even the wrong band gap that the band gap is less than 0 eV for semiconductors with impurities. To improve the accuracy of electronic structures, quasiparticle energies are obtained using *GW* approximation. By comparing the electronic structure calculated by DFT, our results of the electronic structure using *GW* approximation are in reasonable agreement with experiments. *GW* method may help understanding the change in the electronic structure of highly correlated transition metal oxide with impurities.

6.2   Outlook

Our results agree with experiments well, *GW* method may widely be used in study transition metal oxides. This thesis is almost exclusively based on *GW* calculation using our original all-electron mixed basis code TOMBO developed by Prof. Kaoru Ohno, *et al.*.

The powerfulness of TOMBO is not only based on *GW* approximation but also based on the fact that it enables us to perform the state-of-the-art calculations such as time-dependent DFT, Self-consistent-*GW* approximation, *GW*+T-matrix method, Bether–Salpeter equation, and an estimation of on-site Coulomb energy for molecular Mott insulator. Using these methods, we expect that TOMBO will solve the problems related to strong electron correlations of transition metal oxides, electronic structure around the band gap, and so forth.

Acknowledgements

First and foremost, I would like to express my deepest gratitude to my advisor, Prof. Kaoru Ohno, for his patient guidance, advice, and providing me with an excellent atmosphere for doing research. He helped me a lot not only in my study, but also in my life. I first came to Japan in 2012, at that time my Japanese was very poor. Prof. Kaoru Ohno greatly helped me integrate into local life. I could not have imagined having a better advisor and mentor for my Ph.D study.

Besides my advisor, I would like to thank Dr. Shota Ono for nice advices and discussions in my reseach.

I would like to thank Mr. Yusuke Noda, our laboratory secretary Mrs. Watanabe and other lab members, they gave me a lot of help during my study.

I would like to thank Prof. Lei Miao and Prof. Sakae Tanemura for advices about TiO_2 experimental works.

Finally, I would also like to thank my parents and two sisters. They were always supporting me and encouraging me.

References

[1] S. P. Kowalczyk, F. R. McFeely, L. Ley, V. T. Gritsyna, and D. A. Shirley. The electronic structure of $SrTiO_3$ and some simple related oxides (MgO, Al_2O_3, SrO, TiO_2). *Solid State Communications*, 23(3):161–169, 1977.

[2] H. Tang, F. Lévy, H. Berger, and P. E. Schmid. Urbach tail of anatase TiO_2. *Phys. Rev. B*, 52(11):7771–7774, 1995.

[3] J. Pascual, J. Camassel, and H. Mathieu. Fine structure in the intrinsic absorption edge of TiO_2. *Phys. Rev. B*, 18(10):5606–5614, 1978.

[4] A. Amtout and R. Leonelli. Optical properties of rutile near its fundamental band gap. *Phys. Rev. B*, 51(11):6842–6851, 1995.

[5] Yasuhisa Tezuka, Shik Shin, Takehiko Ishii, Takeo Ejima, Shoji Suzuki, and Shigeru Sato. Photoemission and bremsstrahlung isochromat spectroscopy studies of TiO_2 (rutile) and $SrTiO_3$. *Journal of the Physical Society of Japan*, 63(1):347–357, 1994.

[6] Sylvie Rangan, Senia Katalinic, Ryan Thorpe, Robert Allen Bartynski, Jonathan Rochford, and Elena Galoppini. Energy level alignment of a Zinc(II) tetraphenyl-porphyrin dye adsorbed onto $TiO_2(110)$ and $ZnO(1120)$ surfaces. *The Journal of Physical Chemistry C*, 114(2):1139–1147, 2010.

[7] P. J. Hardman, G. N. Raikar, C. A. Muryn, G. van der Laan, P. L. Wincott, G. Thornton, D. W. Bullett, and P. A. D. M. A. Dale. Valence-band structure of tio_2 along the γ-δ-X and γ-σ-M directions. *Phys. Rev. B*, 49(11):7170–7177, 1994.

[8] C. Kittel. *Introduction to Solid State Physics, 6th ed.* Wiley, 1986.

[9] A. Mang, K. Reimann, and St. Rübenacke. Band gaps, crystal-field splitting, spin-orbit coupling, and exciton binding energies in ZnO under hydrostatic pressure. *Solid State Communications*, 94(4):251–254, 1995.

[10] P. Hohenberg and W. Kohn. Inhomogeneous electron gas. *Phys. Rev.*, 136(3B):B864–B871, 1964.

[11] John W. DeFord and Owen W. Johnson. Electron transport properties in rutile from 6 to 40 K. *Journal of Applied Physics*, 54, 1983.

[12] D. Morris, Y. Dou, J. Rebane, C. E. J. Mitchell, R. G. Egdell, D. S. L. Law, A. Vittadini, and M. Casarin. Photoemission and STM study of the electronic structure of Nb-doped TiO_2. *Phys. Rev. B*, 61:13445–13457, 2000.

[13] J. P. Perdew and Alex Zunger. Self-interaction correction to density-functional approximations for many-electron systems. *Phys. Rev. B*, 23:5048–5079, 1981.

[14] U. Salzner, P. G. Pickup, R. A. Poirier, and J. B. Lagowski. Accurate method for obtaining band gaps in conducting polymers using a DFT/Hybrid approach. *J. Phys. Chem. A*, 102:2572, 1998.

[15] I. V. Solovyev, P. H. Dederichs, and V. I. Anisimov. Corrected atomic limit in the local-density approximation and the electronic structure of *d* impurities in rb. *Phys. Rev. B*, 50:16861–16871, 1994.

[16] Michael Nolan, Simon D. Elliott, James S. Mulley, Roger A. Bennett, Mark Basham, and Paul Mulheran. Electronic structure of point defects in controlled self-doping of the TiO_2 (110) surface: Combined photoemission spectroscopy and density functional theory study. *Phys. Rev. B*, 77:235424, 2008.

[17] Lars Hedin. New method for calculating the one-particle Green's function with application to the electron-gas problem. *Phys. Rev.*, 139(3A):A796–A823, 1965.

[18] Mark S. Hybertsen and Steven G. Louie. Electron correlation in semiconductors and insulators: Band gaps and quasiparticle energies. *Phys. Rev. B*, 34(8):5390–5413, 1986.

[19] R. W. Godby, M. Schlüter, and L. J. Sham. Self-energy operators and exchange-correlation potentials in semiconductors. *Phys. Rev. B*, 37(17):10159–10175, 1988.

[20] Wei Kang and Mark S. Hybertsen. Quasiparticle and optical properties of rutile and anatase TiO_2. *Phys. Rev. B*, 82(8):085203, 2010.

[21] Christopher E Patrick and Feliciano Giustino. *GW* quasiparticle bandgaps of anatase TiO_2 starting from DFT+*U*. *Journal of Physics: Condensed Matter*, 24(20):202201, 2012.

[22] M. Oshikiri, M. Boero, F. Aryasetiawan J. Ye, and G. Kido. The electronic structures of the thin films of $InVO_4$ and TiO_2 by first principles calculations. *Thin Solid Films*, 445(2):168–174, 2003.

[23] Letizia Chiodo, Juan Maria Garcia-Lastra, Amilcare Iacomino, Stefano Ossicini, Jin Zhao, Hrvoje Petek, and Angel Rubio. Self-energy and excitonic effects in the electronic and optical properties of TiO_2 crystalline phases. *Phys. Rev. B*, 82(4):045207, 2010.

[24] M. van Schilfgaarde, Takao Kotani, and S. Faleev. Quasiparticle self-consistent *GW* theory. *Phys. Rev. Lett.*, 96(22):226402, 2006.

[25] T. Kotani, M. van Schilfgaarde, S. V. Faleev, and A. Chantis. Quasiparticle self-consistent *GW* method: a short summary. *J. Phys. : Condens. Matter*, 19(36):365236, 2007.

[26] Stephan Lany. Band-structure calculations for the 3*d* transition metal oxides in *GW*. *Phys. Rev. B*, 87(8):085112, 2013.

[27] M. Shishkin and G. Kresse. Self-consistent *GW* calculations for semiconductors and insulators. *Phys. Rev. B*, 75(23):235102, 2007.

[28] M. Shishkin, M. Marsman, and G. Kresse. Accurate quasiparticle spectra from self-consistent *GW* calculations with vertex corrections. *Phys. Rev. Lett.*, 99(24):246403, 2007.

[29] Michael Rohlfing and Steven G. Louie. Electron-hole excitations and optical spectra from first principles. *Phys. Rev. B*, 62:4927–4944, Aug 2000.

[30] Giovanni Onida, Lucia Reining, and Angel Rubio. Electronic excitations: density-functional versus many-body green's-function approaches. *Rev. Mod. Phys.*, 74:601–659, Jun 2002.

[31] Mark S. Hybertsen and Steven G. Louie. First-principles theory of quasiparticles: Calculation of band gaps in semiconductors and insulators. *Phys. Rev. Lett.*, 55:1418–1421, Sep 1985.

[32] Wolfgang von der Linden and Peter Horsch. Precise quasiparticle energies and hartree-fock bands of semiconductors and insulators. *Phys. Rev. B*, 37:8351–8362, May 1988.

[33] Kaoru Ohno, Francesco Mauri, and Steven G. Louie. Magnetic susceptibility of semiconductors by an all-electron first-principles approach. *Phys. Rev. B*, 56(3):1009–1012, 1997.

[34] Tsutomu Ohtsuki, Kaoru Ohno, Keiichiro Shiga, Yoshiyuki Kawazoe, Yutaka Maruyama, and Kazuyoshi Masumoto. Insertion of Xe and Kr atoms into C_{60} and C_{70} fullerenes and the formation of dimers. *Phys. Rev. Lett.*, 81:967–970, Aug 1998.

[35] S. Ono, Y. Noguchi, R. Sahara, Y. Kawazoe, and K. Ohno. Tombo: All-electron mixed-basis approach to condensed matter physics. *Computer Phys. Comm.*, 189:20–30, 2015.

[36] K. Ohno, S. Ono, R. Kuwahara, Y. Noguchi, R. Sahara, Y. Kawazoe, and M. H. F. Sluiter. **TOMBO Group**. *http://www.ohno.ynu.ac.jp/tombo/index.html*.

[37] Soh Ishii, Kaoru Ohno, Yoshiyuki Kawazoe, and Steven G. Louie. *Ab initio GW* quasiparticle energies of small sodium clusters by an all-electron mixed-basis approach. *Phys. Rev. B*, 63(15):155104, 2001.

[38] Erm Kikuchi, Shohei Iwata, Soh Ishii, and Kaoru Ohno. First-principles *GW* calculations of gaas clusters and crystal using an all-electron mixed basis approach. *Phys. Rev. B*, 76(7):075325, 2007.

[39] Soh Ishii, Shohei Iwata, and Kaoru Ohno. All-electron *GW* calculations of silicon, diamond, and silicon carbide. *Materials Transactions*, 51(12):2150–2156, 2010.

[40] Lars Hedin and Stig Lundqvist. Effects of electron-electron and electron-phonon interactions on the one-electron states of solids. volume 23 of *Solid State Physics*, pages 1 – 181. Academic Press, 1970.

[41] Kaoru Ohno, Keivan Esfarjani, and Yoshiyuki Kawazoe. *Computational materials science: from ab initio to Monte Carlo methods*, volume 129. Springer-Verlag, Berlin and Heidelberg, 1999; see Fig. 2.23 on p.113.

[42] Mark S. Hybertsen and Steven G. Louie. Theory of quasiparticle surface states in semiconductor surfaces. *Phys. Rev. B*, 38:4033–4044, Aug 1988.

[43] R. W. Godby, M. Schlüter, and L. J. Sham. Accurate exchange-correlation potential for silicon and its discontinuity on addition of an electron. *Phys. Rev. Lett.*, 56:2415–2418, Jun 1986.

[44] R. W. Godby, M. Schlüter, and L. J. Sham. Quasiparticle energies in gaas and alas. *Phys. Rev. B*, 35:4170–4171, Mar 1987.

[45] R. W. Godby, M. Schlüter, and L. J. Sham. Trends in self-energy operators and their corresponding exchange-correlation potentials. *Phys. Rev. B*, 36:6497–6500, Oct 1987.

[46] S. Ishii and K. Ohno. Full-ω integration *GW* calculation of Ne atom. unpublished.

[47] W. Kohn and L. J. Sham. Self-consistent equations including exchange and correlation effects. *Phys. Rev.*, 140:A1133–A1138, 1965.

[48] S.F. Boys and F. Bernardi. The calculation of small molecular interactions by the differences of separate total energies. some procedures with reduced errors. *Mol. Phys.*, 19:553, 1970.

[49] B. Liu and A.D. McLean. Accurate calculation of the attractive interaction of two ground state helium atoms. *J. Chem. Phys.*, 59:4557, 1973.

[50] K. Pachucki and J. Komasa. Gaussian basis sets with the cusp condition. *Chem. Phys. Lett.*, 389:209, 2004.

[51] S. X. Zhang, D. C. Kundaliya, W. Yu, S. Dhar, S. Y. Young, L. G. Salamanca-Riba, S. B. Ogale, R. D. Vispute, and T. Venkatesan. Niobium doped TiO_2: Intrinsic transparent metallic anatase versus highly resistive rutile phase. *Journal of Applied Physics*, 102(1):–, 2007.

[52] S. C. Abrahams and J. L. Bernstein. Rutile: Normal probability plot analysis and accurate measurement of crystal structure. *The Journal of Chemical Physics*, 55(7), 1971.

[53] G. Kresse and J. Hafner. *Ab initio* molecular dynamics for liquid metals. *Phys. Rev. B*, 47:558–561, 1993.

[54] G. Kresse and J. Furthmüller. Efficiency of ab-initio total energy calculations for metals and semiconductors using a plane-wave basis set. *J. Comput. Mater. Sci.*, 6:15, 1996.

[55] D. C. Cronemeyer. Electrical and optical properties of rutile single crystals. *Phys. Rev.*, 87:876–886, 1952.

[56] The PPM von der Linden-Horsch was implemented in our all-electron GW mixed basis code by R. Kuwahara and K. Ohno; see, for example, R. Kuwahara, Y. Tadokoro, and K. Ohno. Validity of virial theorem in all-electron mixed basis density functional Hartree-Fock, and GW calculations. J. Chem. Phys. 141(8):084108, 2014; R. Kuwahara and K. Ohno. Linearized self-consistent GW approach satisfying the Ward identity. Phys. Rev. A, 90(3):032506, 2014.